TECHNISCHE UNIVERSITÄT WIEN

ACIN AUTOMATION & CONTROL INSTITUTE INSTITUT FÜR AUTOMATISIERUNGS- & REGELUNGSTECHNIK

Laser speckle-based sensor for in-plane displacement sensing

DIPLOMARBEIT

Ausgeführt zum Zwecke der Erlangung des akademischen Grades eines
Diplom-Ingenieurs (Dipl.-Ing.)

unter der Leitung von

Associate Prof. Dr.techn. Ernst Csencsics
Dipl.-Ing. Matthias Laimer

eingereicht an der
Technischen Universität Wien
Fakultät für Elektrotechnik und Informationstechnik
Institut für Automatisierungs- und Regelungstechnik

von

Tobias Wolf, BSc.
Matrikelnummer: 01526109

Wien, im März 2024

Advanced Mechatronic Systems Group
Gußhausstrasse 27-29, A-1040 Wien, Internet: http://www.acin.tuwien.ac.at

Acknowledgements

I am immensely grateful to everyone who has been part of my academic journey and has contributed to the successful completion of my master's thesis. Firstly, I want to thank my supervisor, Associate Prof. Dr.techn. Ernst Csencsics, for his effort and sharing his knowledge over the whole course of this thesis, and for his empathy during a challenging time in my life. Next, I want to thank my second supervisor Dipl.-Ing. Matthias Laimer, for his effort and assistance in the laboratory, many constructive discussions, and for proofreading my thesis.

Furthermore, I am grateful to Univ.-Prof. Dr.sc.techn. Georg Schitter for providing me with the opportunity to undertake this thesis and to every other member of the Advanced Mechatronic Systems (AMS) group, who participated in some way by sharing their knownledge.

I also want to thank my friends and colleagues for their support, motivation, and shared experiences throughout this journey.

Lastly, I want to express my deepest gratitude to my family and especially my parents, Bettina and Manfred, for their unwavering support, encouragement, and the efforts that have made my studies possible. Their belief in me has been my greatest motivation.

Thank you!

Abstract

Laser speckle-based in-plane displacement sensors offer several desirable properties, such as a simple setup, contactless measurements, and high resolution. However, they have been limited in their measurement range in the past. Overcoming this limitation in recent research has led to renewed interest in the measurement principle in various fields, including applications in robotic manufacturing and vehicle odometry. Due to rising demands for precision and increasing measurement rates, this master's thesis focuses on the development of a high speed and high resolution laser speckle-based in-plane displacement sensor. In order to achieve compactness, the sensor utilizes an objective laser speckle-based setup, facilitating easy sensor integration into various systems. Speckle images are captured using a line sensor rather than traditional 2D image sensors, offering advantages such as enhanced frame rates and reduced computational effort due to the processing of fewer pixels. Geometric considerations are conducted to maximize sensitivity for in-plane displacements in one degree of freedom, while minimizing crosstalk for the remaining translational degrees of freedom. Pixel data acquisition and processing are performed using a FPGA board, with the program based on a comprehensive timing analysis. Through the implementation of a pipelined program architecture, multiple tasks are executed in parallel, thus optimizing the measurement rate of the sensor. Additionally, subpixel interpolation methods are employed to enhance the sensor resolution. Experimental results demonstrate a resolution of 3.5 μm, a measurement rate of 24.72 kHz, and a low sensor latency of 72.35 μs. These findings highlight the effectiveness of the proposed sensor prototype and its potential for high speed and high resolution in-plane displacement measurements for future industrial applications.

Zusammenfassung

Laser-Speckle-basierte In-Plane-Verschiebungssensoren bieten vielversprechende Eigenschaften, wie einen einfachen Aufbau, berührungslose Messungen und eine hohe Auflösung. In der Vergangenheit waren sie jedoch in ihrem Messbereich begrenzt. Die Überwindung dieser Limitierung innerhalb der letzten 10 Jahre, hat zu einem erneuten Interesse an dem Messprinzip in verschiedenen Bereichen geführt, einschließlich Anwendungen in der Roboterfertigung und der Odometrie. Aufgrund steigender Anforderungen nach Präzision und höheren Messraten konzentriert sich diese Masterarbeit auf die Entwicklung eines hochgeschwindigkeits- und hochauflösenden Laser-Speckle-basierten In-Plane-Verschiebungssensors. Um eine kompakte Bauweise zu erreichen, verwendet der Sensor einen objektiven Laser-Speckle-basierten Aufbau, der eine einfache Integration des Sensors in verschiedene Systeme ermöglicht. Speckle-Bilder werden mit einem Zeilensensor statt mit herkömmlichen 2D-Bildsensoren erfasst, was Vorteile wie höhere Bildraten und einen geringeren Rechenaufwand bietet. Geometrische Überlegungen werden angestellt, um die Empfindlichkeit für Verschiebungen in der Ebene in einem Freiheitsgrad zu maximieren und gleichzeitig den Einfluss durch die übrigen translatorischen Freiheitsgrade zu minimieren. Die Erfassung und Verarbeitung der Pixeldaten erfolgt über einen FPGA. Durch die Implementierung einer Pipeline-Programmarchitektur können mehrere Aufgaben parallel ausgeführt werden, wodurch die Messrate des Sensors optimiert wird. Zusätzlich werden Subpixel-Interpolationsalgorithmen eingesetzt, um die Auflösung des Sensors weiter zu verbessern. Experimentelle Ergebnisse zeigen eine Auflösung von 3.5 μm und eine Messrate von 24.72 kHz, bei nur geringer Zeitverzögerung von 72.35 μs. Diese Ergebnisse unterstreichen die Effektivität des entwickelten Sensorprototyps und sein Potenzial für Hochgeschwindigkeits- und hochauflösende in-plane Verschiebungsmessungen für zukünftige industrielle Anwendungen.

Contents

List of Figures

List of Tables

Acronyms

ADC Analog Digital Converter

AO Anaolg Output

CC Cross Correlation

CCD Charge-Coupled Device

CMOS Complementary Metal-Oxide-Semiconductor

DI Digital Input

DIC Digital Image Correlation

DoF Degree of Freedom

DSP Digital Signal Processor

ESD Electrostatic Discharge

ESPI Electronic Speckle Pattern Interferometry

FFT Fast Fourier Transformation

FPGA Field Programmable Gate Array

GPIOs General Purpose Inputs Outputs

LSA Localized Spectrum Analysis

LSB Least Significant Bit

LUT Lookup Table

OLSP Objective Laser Speckles

PCB Printed Circuit Board

PZT Piezoelectric Transducer

SLSP Subjective Laser Speckles

SPI Serial Peripheral Interface

SSD Sum of Squared Distances

ZNCC Zero Normalised Cross Correlation

ZNSSD Zero Normalised Sum of Squared Distances

CHAPTER 1

Introduction

High-tech industrial manufacturing systems are experiencing a persistent rise in the need for precision and throughput [1]. In response, particular attention is paid to the integration of fast, accurate and reliable sensor systems directly into the production line [2, 3].

1.1 Motivation

While numerous optical sensor principles have been developed for measuring out-of-plane displacement in the past [4], techniques for measuring in-plane displacement are notably limited. Existing methods rely on optically resolvable macroscopic structure and often utilize marker-based approaches, applying either artificially created speckle [5, 6] or checkerboard patterns [7–9] onto the object. These markers are then captured with an image sensor to determine in-plane displacement. While the measurment principle is easy to deploy, it suffers from significant disadvantages. The markers used for tracking may experience cracking, peeling, oxidation and fading under external mechanical or thermal loads, which can adversely affect image quality and introduce errors [10]. Additionally, attaching markers to every object is impractical, especially when considering the demand for high throughput.

Another method for measuring in-plane displacements involves interferometric principles, commonly referred to as Electronic Speckle Pattern Interferometry (ESPI) [11]. While this method has a resolution in the nanometer scale, the setup becomes complex, and the measurement range is often limited to below 10 μm [12].

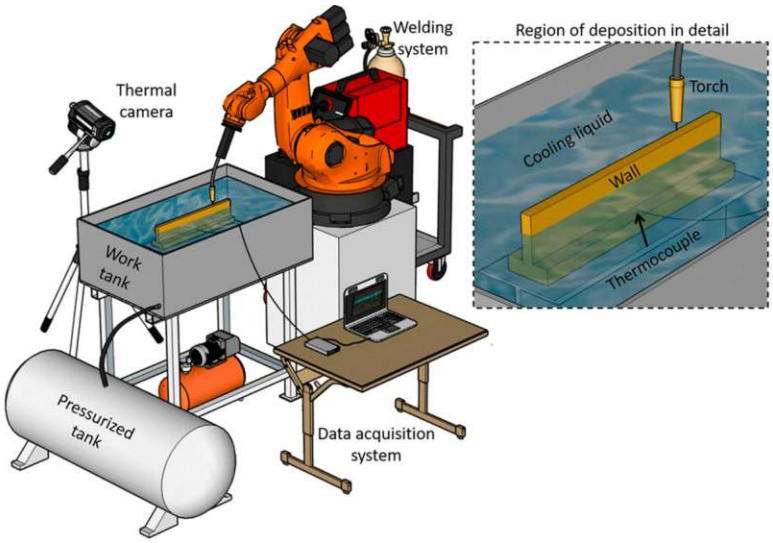

Figure 1.1: Robotic wire and arc additive manufacturing [24].

One of the most promising approaches for measuring in-plane displacements is through laser speckle correlation-based measurement [13]. This method offers desirable properties such as a simple setup and contactless and high resolution measurements [14] on various technical surfaces without the need for artifical markers [15]. Compared to interferometric principles, non-interferometric laser speckle-based measurement methods offer a more compact setup, allowing for an easy sensor integration into various systems. However, two persistent challenges remain: a limited measurement range due to decorrelation effects [16] and a limited measurement rate due to complexity of image processing, especially for high resolution images. As a result, laser speckle-based sensor systems have primarily been utilized for in-plane strain measurements in the past [17, 18]. Recently, significant improvements have been made to overcome the limited measurement range. For large in-plane displacements the measurement range can be increased by resetting the reference image if correlation drops below a certain value [19] or by a compensation-based system, which actively tracks the object displacement [13]. These improvements have led to a renewed interest in the measurment priciple with researchers investigating its potential in various fields, including applications in robotic manufacturing [13, 19, 20] and vehicle odometry [21–23]. Figure 1.1 shows a typical setup for robotic wire and arc additive manufacturing. Here, the utilization of a laser speckle-based sensor for compensating velocity errors has the potential of enhancing process quality [19, 20].

Another specific application case in industrial manufacturing, are object inspection tasks directly in the production line [25–27]. Environmental vibrations or object

movements can lead to relative motion between the inspection tool and the object. Therefore, it is necessary to measure displacements and track the object to maintain a constant position of the inspection tool relative to the object [13]. Aiming for satisfying the demands of high-tech industrial manufacturing systems, such as high throughput [1] and fast, accurate and reliable measurement systems [2, 3], recent research initiatives have tackled this challenge. One approach employs a six Degree of Freedom (DoF) MAGLEV positioning platform, capable of tracking in- and out-of-plane object displacements with submicrometer precision and control bandwidths of up to 450 Hz with a marker-based principle [28–31]. While the high control bandwidth allows for compensation of in- and out-of-plane object vibrations, the disadvantage is that laser markers have to be applied to the object. Another approach involves a speckle-based measurement system capable of tracking both out-of-plane and in-plane displacements with single micrometer resolution [13]. However, its low measurement rate of 10 Hz significantly restricts the control bandwidth. Hence, further research aiming at enhancing the measurement rate of speckle-based displacement sensors holds the potential of overcoming this limitation and further elevating the capabilities of industrial manufacturing systems.

1.2 Aim of the Thesis

Motivated by the need for high resolution and high speed in-plane displacement sensors this thesis aims to explore the intricacies of laser speckle-based in-plane displacement sensors. Significant research efforts have enhanced the resolution of digital image correlation methods [32–34], consequently improving the resolution of laser speckle-based in-plane displacement sensors. However, there has been limited focus on increasing the measurement rates of such sensors so far. Investigating existing laser speckle-based in-plane displacement sensors reveals that they typically operate at measurement rates between 10 and 100 Hz [13, 21]. Major challenges for increasing the measurement rate of these sensors lie in the development of a real-time communication interface with minimal latency.

Therefore, the aim of this thesis is to develop a laser speckle-based in-plane displacement sensor capable of measuring with single micrometer resolution and measurement rates up to several 10 kHz. Accomplishing this aim requires appropriate hardware and prioritizing fast image data acquisition and processing. Specific tasks include developing a real-time software interface for reading out the image sensor and implementing fast and accurate image processing methods to detect in-plane displacements with subpixel accuracy and minimal latency. Additionally, a thorough evaluation of the speckle-based in-plane displacement sensor is required. The objectives can be summarized as follows:

- Development of a high resolution and high speed laser speckle-based in-plane displacement sensor
- Development of a real-time communication interface
- Implementation of fast and precise algorithms for image processing with minimal latency
- Experimental evaluation of the designed in-plane displacement sensor

1.3 Outline

In this thesis a laser speckle-based in-plane displacement sensor is designed and developed. The performance of the in-plane displacement sensor is experimentally evaluated. Chapter 2 provides an overview of state-of-the-art methods and related research topics for measuring in-plane displacements. Specifically focusing on laser speckle-based systems, it explores techniques for image processing, including methods to achieve subpixel resolution, and strategies for extending the range of motion. In Chapter 3, the focus is on the design and development of a laser speckle-based displacement sensor prototype. This involves addressing geometric considerations, conducting simulations, defining requirements, and selecting components to accomplish the targeted development of a fast and high-precision in-plane displacement sensor. Chapter 4 describes the development of an FPGA program for reading out the image sensor, followed by image processing. The measurement rate of the sensor prototype is optimized through a comprehensive timing analyses. The performance of the speckle-based displacement sensor, including a comparison with a reference measurement taken by a capacitive sensing principle, is evaluated in Chapter 5. Finally, a conclusion and outlook towards possible improvements is presented in Chapter 6.

CHAPTER 2

State of the Art

This chapter provides an overview of the state of the art in optical measurement principles for in-plane displacement sensing, with a focus on laser speckle-based techniques, which offer contactless and high-resolution measurements [14] on various technical surfaces without the need for artifical markers [15]. Additionally, the chapter explores multiple image processing methods to determine in-plane displacements with subpixel resolution, as well as strategies for extending the measurement range of such speckle-based sensors. Finally, the chapter is concluded by defining reasearch questions concerning the feasibility of achieving high measurement rates while maintaining high resolution for laser speckle-based in-plane displacement sensors.

2.1 Optical measurement principles for in-plane displacement sensing

In this section, an overview of optical measurement principles used for in-plane displacement sensing, covering both marker-based sensing and laser speckle-based sensing techniques, is given. While marker-based sensing involves the attachement of physical markers onto the object [5–9], laser speckle-based sensing relies on the analysis of laser speckle pattern and is further divided into non-interferometric and interferometric setups [35]. Additionally, the advantages and disadvantages of each technique are explored to provide insights into their capabilities and limitations.

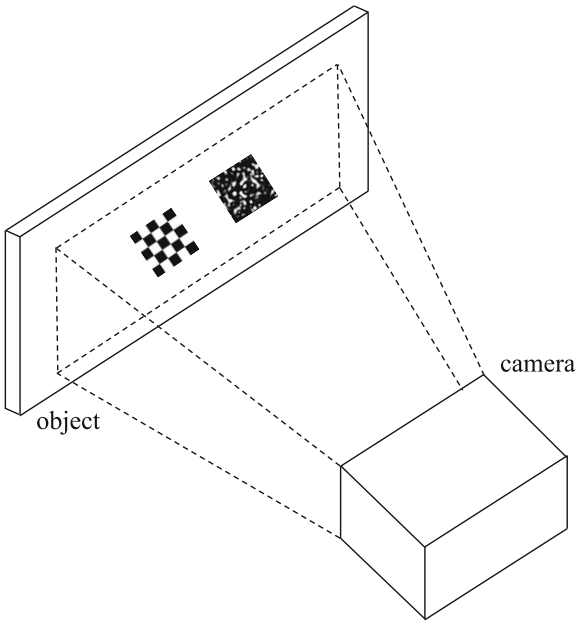

Figure 2.1: Marker-based sensing. Physical markers, such as speckle or checkerboard pattern, are attached to the object. In-plane object displacement is deteremined through the observation of the markers with a camera.

2.1.1 Marker-based sensing

Existing methods for measuring in-plane displacements often utilize marker-based approaches, where either artificial speckle [5, 6] or checkerboard pattern are attached onto the object surface [7–9], as shown in Figure 2.1. These markers are then captured using an image sensor, followed by subsequent image post-processing to determine the displacement. In the case of speckle pattern, the displacement is typically determined through Digital Image Correlation (DIC), involving the solution of optimization problems in either the spatial or frequency domain [36]. The accuracy and precision of marker-based measurements heavily relies on both correlation algorithms and the quality of the fabricated speckle pattern [5]. Consequently, various methods have been developed for artificially creating speckle pattern, such as spraying, airbrushing, spin coating, compressed air technique, nano-film remodeling, and focused ion beam, as discussed in [5].

In the case of periodic checkerboard patterns, in-plane displacements cannot be reliably detected through DIC due to the inherent periodicity of checkerboard patterns [7]. Instead, displacements are determined based on Localized Spectrum Analysis (LSA), which involves solving optimization problems in the frequency domain [7]. Recent research suggests that correctly sampled checkerboard patterns

can provide optimal results for in-plane displacement measurements due to the maximum image gradient they offer [9]. Interestingly, numerical simulations in [7] even indicate that checkerboard patterns may offer resolution superior to that of speckle-based patterns analyzed with DIC.

However, marker-based sensing comes with significant drawbacks. Marker-based principles are not always feasible, particularly for inline metrology applications where high throughput is desired and applying markers to every object is impractical. Additionally, markers are prone to various issues such as cracking, peeling, oxidation and fading when exposed to external mechanical or thermal stresses, all contributing to decreased image quality and increased measurment uncertainty [10].

2.1.2 Laser speckle-based sensing

While for marker-based sensing, speckle or checkerboard pattern are attached to the object, laser speckle-based sensing creates a speckle pattern by illuminating the object and observing the scatterd laser light. This eliminates the drawbacks associated with marker-based sensing. Laser speckles occur when coherent light strikes an optically rough surface or propagates through a medium with random fluctuations of the refractive index [35]. This results in an negative exponential intensity distributions in the scattered/propagated light, which is nowadays referred to as speckle patterns [35]. A typical example is shown in Figure 2.2. It visualizes a granular spatial structure [37], which was first mentioned by early workers in the laser field [38, 39]. Each speckle image is unique to a particular object position, making it well-suited for measuring displacements [15]. Moreover, laser speckle-based measurement systems can be designed in both non-interferometric and interferometric setups [35]. The key distinction lies in the number of laser beams used: in non-interferometric setups, the object is illuminated by a single laser beam, while in interferometric setups, the object is typically illuminated by two beams inclined at equal and opposite angles to the object normal.

2.1.2.1 Non-interferometric setup

According to [35], laser speckles can be mathematically defined by first and second order statistics. While first order statistics focus mainly on the probability density function of the intensity and the speckle contrast, second order statistics describe the autocorrelation function and power spectral density of such patterns [35]. This is of great importance as the width of the normalized autocorrelation function correlates with the speckle size [40, 41]. A comprehensive description of the first and second order statistics goes back to Goodman [37]. To determine the probability

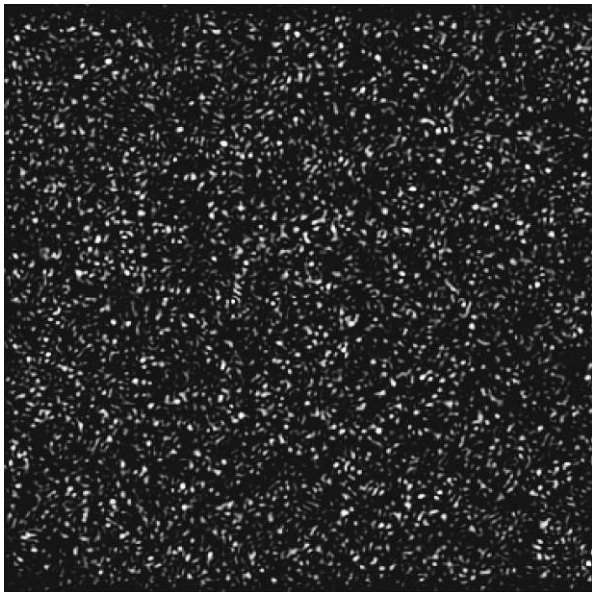

Figure 2.2: Typical speckle pattern with an negative exponential intensity distribution.

density function of the intensity and the speckle contrast, perfectly polarized and perfectly monochromatic light is assumed [42]. Therefore the electromagnetical field at the position (x, y, z) can the be written as

$$E(x, y, z, t) = A(x, y, z)e^{-i\omega t}, \tag{2.1}$$

with $A(x, y, z)$ beeing the complex amplitude of the field and ω beeing the frequency. With the wave vector $k = (k_x, k_y, k_z)^T$ the complex amplitude is represented by

$$A(x, y, z) = |A(x, y, z)|e^{i(k_x x + k_y y + k_z z)}, \tag{2.2}$$

which results in the intensity

$$I(x, y, z) = \lim_{T\to\infty} \frac{1}{T} \int_{-T/2}^{T/2} |E(x, y, z, t)|^2 \, dt = |A(x, x, z)|^2. \tag{2.3}$$

In order to further analyze the intensity, a interpretation of $A(x, y, z)$ according to the object surface is neccessary. As shown in Figure 2.3a and 2.3b, a laser source illuminates a circular area of the object with a diameter D. The rough surface can be divided in multiple scattering areas, representing the micro-structure of the object [13]. This results in diffuse reflexion of the laser light. For the free-space geometry in Figure 2.3a, also called Objective Laser Speckles (OLSP), every scatter

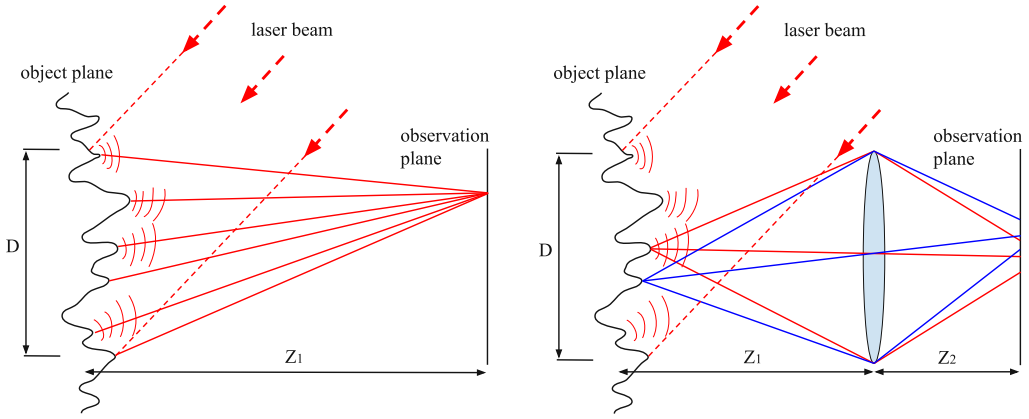

(a) (b)

Figure 2.3: Image formation for free-space and lens geometry [43]. The incoming laser light is scattered at every surface point. (a) Every illuminated surface point can influence the intensity at a given observation point. (b) A certain surface point can only influence the intensity within a limited area on the observation plane. The size of the area depends on the distance z_2 from the lens to the obseravtion plane and the focal length of the lens. The resolution limit is given by the Airy disc [44].

influences the intensity at a given observation point. For the lens-included geometry in Figure 2.3b, also called Subjective Laser Speckles (SLSP), the possible area at the observation plane is limited for every scatter. If the distance z_2 between the observation plane and lens equals the focal length of the lens, the system can theoretically resolve the elementary scattering areas [42]. However, in most practical applications, the number of scattering areas N influencing an observation point on the obseravtion plane is large [42]. Therfore the complex amplitude of the field at the position (x, y, z) can be interpreted as summation over N complex amplitudes of the scattering areas, as shown in Figure 2.4. This is written as

$$A(x, y, z) = \sum_{k=1}^{N} |a_k| e^{i\phi_k} \tag{2.4}$$

where $|a_k|$ and ϕ_k are the amplitude and phase of the k-th scattering area. Goodman [37, 42] further describes the complex summation as a classical random walk phenomenon with two assumptions. First, $|a_k|$ and ϕ_k are statistically independent of each other, and independent from the amplitude and phase of all other scatters. The phases ϕ_k are uniformly distributed within -π and π. This restriction to values between -π and π does not pose a limitation, due to 2π periodicity. With these

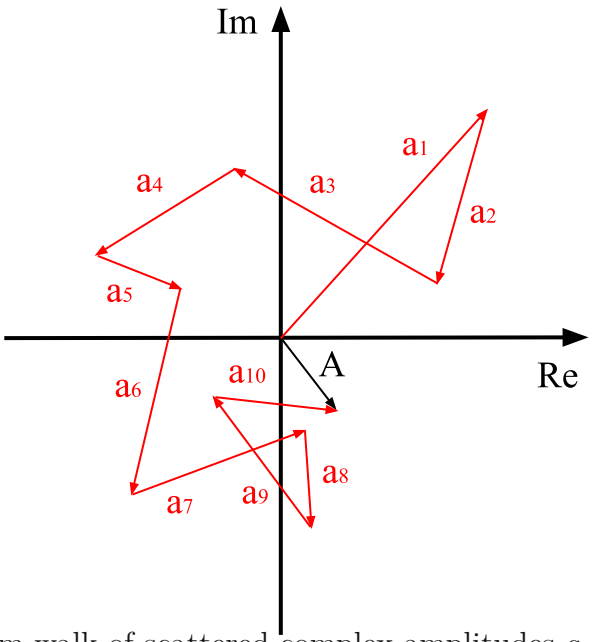

Figure 2.4: Random walk of scattered complex amplitudes a_k [42]. The phase of each scatter is uniformly distributed between -π and π. Therfore the resulting summed amplitude $|A|$ tends to smaller values, leading to a negative expotenitial form of the probability density function of the intensity.

assumtions, the probability density function of the intensity

$$p(I) = \begin{cases} \frac{1}{\bar{I}} e^{\frac{-I}{\bar{I}}}, & I \geq 0 \\ 0, & I < 0 \end{cases} \tag{2.5}$$

has a negative exponential trend, with $\bar{I}$ beeing the mean intensity. As a result of the negative exponential propability decrease for rising intensities, bright spots are less likely to appear than dark spots. The probabilty that the intensity is bigger than a threshold I_T is given by

$$p(I > I_T) = \begin{cases} e^{-\frac{I_T}{\bar{I}}}, & I_T \geq 0 \\ 1, & I_T < 0. \end{cases} \tag{2.6}$$

The contrast of a speckle pattern results in

$$C = \frac{\sigma_I}{\bar{I}}, \tag{2.7}$$

where σ_I is the standard diviation of the intensity. As a result of the negative exponential probability density function of the intensity, σ_I equals $\bar{I}$. Therefore,

the contrast equals unity [42]. Another important property of speckle pattern is the mean speckle size. A derivation for free-space propagation using second-order statistics is given in [41]. Again, monochromatic light and an optically rough surface are assumed. In this scenario, determining the mean speckle size can be achieved by utilizing the normalized autocorrelation function of the speckle intensity at the observation plane. For the two points $I(x_1, y_1)$ and $I(x_2, y_2)$ in the observation plane, the normalized autocorrelation function is defined as

$$C(\Delta x, \Delta y) = \langle I(x_1, y_1) I(x_2, y_2) \rangle \tag{2.8}$$

with $\Delta x = x_2$ - x_1 and $\Delta y = y_2$ - y_1. This can be further written as

$$C(\Delta x, \Delta y) = \bar{I}^2 \left(1 + \left| \frac{\int_{-\infty}^{\infty} \int_{-\infty}^{\infty} I(u,v)^2 exp(\frac{i2\pi}{\lambda z_1}(u\Delta x + v\Delta y))\, du\, dv}{\int_{-\infty}^{\infty} \int_{-\infty}^{\infty} I(u,v)^2\, du\, dv} \right|^2 \right), \tag{2.9}$$

where λ is the laser wavelength, z_1 is the distance between the object and the observation plane and the double integral $\int_{-\infty}^{\infty} \int_{-\infty}^{\infty}$ represents integration over the surface of the observation plane. [41]. With the assumption of a circular laser spot with a diameter D on the object, Equation 2.9 reduces to

$$C(\Delta x, \Delta y) = \bar{I}^2 \left(1 + \frac{\left(\frac{D}{2}\right)^3}{\lambda z_1} \left| \frac{J_1\left(\frac{\pi D}{\lambda z_1}\sqrt{\Delta x^2 + \Delta y^2}\right)}{\sqrt{\Delta x^2 + \Delta y^2}} \right|^2 \right), \tag{2.10}$$

where J_1 is the first order Bessel function [41]. The mean speckle size can be determined as the value $\sqrt{\Delta x^2 + \Delta y^2}$ at which the first order bessel function J_1 first equals zero, occurring when its argument equals 1.22π [41]. Consequently, the mean speckle size is determined by

$$s_{obj} = \frac{1.22 \lambda z_1}{D}. \tag{2.11}$$

Equation 2.11 illustrates that the mean speckle size s_{obj} expands linearly with the distance from the object to the observation plane, while it decreases for rising laser diameters D. For the subjective case the mean speckle size is written as

$$s_{subj} = 1.22 \lambda \frac{F(1+M)}{a}, \tag{2.12}$$

where F is the focal length of the lens, M is the magnification of z_2/z_1 and a is the lens diameter [44]. By using first and second-order statistics the speckle pattern is characterized according to intensity distribution, contrast and mean speckle size for a static OLSP and SLSP setup.

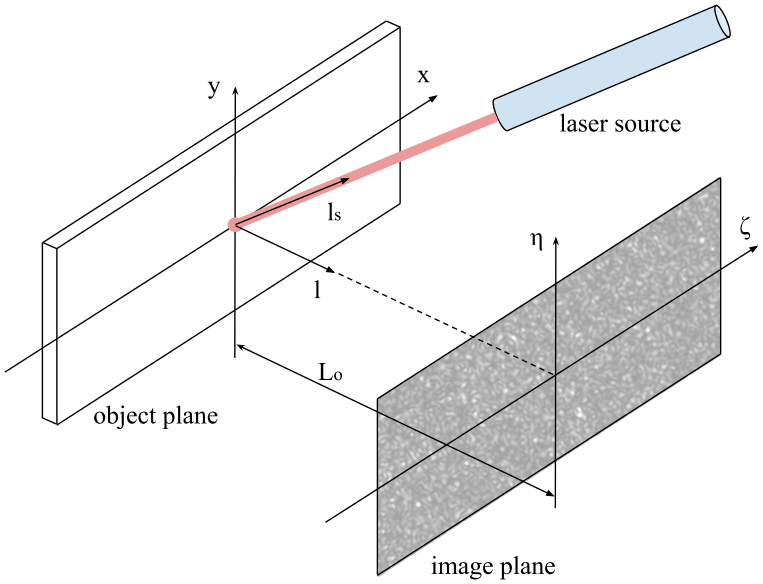

Figure 2.5: Objective laser speckle setup [46]. An optically rough object is illuminated by a laser source. An image sensor captures the resulting speckle pattern. Object translations, rotations and strain lead to speckle shifts in ζ- and η-direction in the image plane.

The description of dynamic processes can be attributed to Yamaguchi [45]. He outlines the changes in speckle patterns resulting from object displacements, rotations, and strain for both free-space and lens-including geometries. Figure 2.5 displays an OLSP setup, with an optically rough object placed at the object plane (x, y) and an image sensor positioned at the image plane (ζ, η) with a distance L_o to the object plane. The object is illuminated by a laser source with a wavelength λ. The source vector $l_s = (l_{sx}, l_{sy}, l_{sz})^T$ represents the direction of the laser source, pointing from the light spot on the object (origin of the object plane) towards the laser. The orientation of the image sensor is denoted by the vector $l = (l_x, l_y, l_z)^T$, pointing from the origin of the object plane towards the center of the image sensor. The vector l is perpendicular to the image plane. Object displacements a_x, a_y, and a_z, object rotations Ω_x, Ω_y, and Ω_z, and object strains ϵ_{xx}, ϵ_{xy}, and ϵ_{yy} lead to speckle shifts in the image plane

$$\begin{aligned} A_\zeta = &- a_x \left(\frac{L_o}{L_s}(l_{sx}^2 - 1) + l_x^2 - 1 \right) - a_y \left(\frac{L_o}{L_s} l_{sx} l_{sy} + l_x l_y \right) - a_z \left(\frac{L_o}{L_s} l_{sx} l_{sz} + l_x l_z \right) \\ &- L_o \Big(\epsilon_{xx}(l_{sx} + l_x) + \epsilon_{xy}(l_{sy} + l_y) + \Omega_z(l_{sy} + l_y) - \Omega_y(l_{sz} + l_z) \Big) \end{aligned} \tag{2.13}$$

and

$$A_\eta = -a_x\left(\frac{L_o}{L_s}l_{sy}l_{sx}+l_y l_x\right)-a_y\left(\frac{L_o}{L_s}(l_{sy}^2-1)+l_y^2-1\right)-a_z\left(\frac{L_o}{L_s}l_{sy}l_{sz}+l_y l_z\right) - L_o\Big(\epsilon_{yy}(l_{sy}+l_y)+\epsilon_{xy}(l_{sx}+l_x)-\Omega_z(l_{sx}+l_x)-\Omega_x(l_{sz}+l_z)\Big) \tag{2.14}$$

where L_s is the radius of curvature at the object [45]. When using this setup as a sensor, the system has 9 inputs (3 for translation, 3 for rotation, and 3 for strain) which are mapped onto the two DoF outputs, A_ς and A_η. The goal of sensor design must, therefore, be to maximize the sensitivity for 2 desired inputs, distributed across the 2 outputs, and minimize the crosstalk for the other 7 inputs. Therefore, it is advisable to use the sensor specifically for detecting either displacements, rotations, or strain, while excluding the other two cases. For further considerations, the setup is intended to measure in-plane displacements. To determine speckle shifts a reference image before and a subimage after translation are recorded and compared by DIC. Due to decorrelation effects, the measurement range and the resolution of OLSP and SLSP systems is limited. According to [16], the normalized correlation factor can be expressed as

$$\delta = \gamma\Omega\Psi \tag{2.15}$$

where γ is the Yamaguchi correlation factor, representing changes in the microstructure. This can occur due to translation, altering the illumination position on the object and, consequently, introducing new scatters, while others are lost. Therefore, the Yamaguchi correlation factor γ is the limiting factor according to the measurement range. The correlation factor Ω defines the fraction of the subimage where an overlap with the reference image may be found. For this reason, the reference image should be bigger than every subsequent image. However, if the translation in x- and y-direction equals half the pixel size, the correlation factor Ω decreases due to sampling errors. Therefore, the correlation factor Ω is the limiting factor according to resolution. The correlation factor Ψ represents the decorrelation effect due to displacement gradients. In order to use a speckle-based sensor for measuring in-plane displacements, displacement gradients, which normally arise from strain, are excluded. Therefore, the correlation factor Ψ becomes 1 and the overall normalized correlation factor δ reduces to $\gamma\Omega$. While the correlation factor γ limits the measurment range, the correlation factor Ω limits the resolution of non-interferometric laser speckle-based displacement sensors. With methods for increasing the measurment range, presented in Section 2.3, and methods for achieving subpixel resolution, discussed in Section 2.2.4, decorrelation effects can be minimized, thereby improving the performance of the measurement principle. Overall non-interferometric laser speckle-based in-plane displacement sensors offer desireable properties, including a simple setup and contactless and high resolution

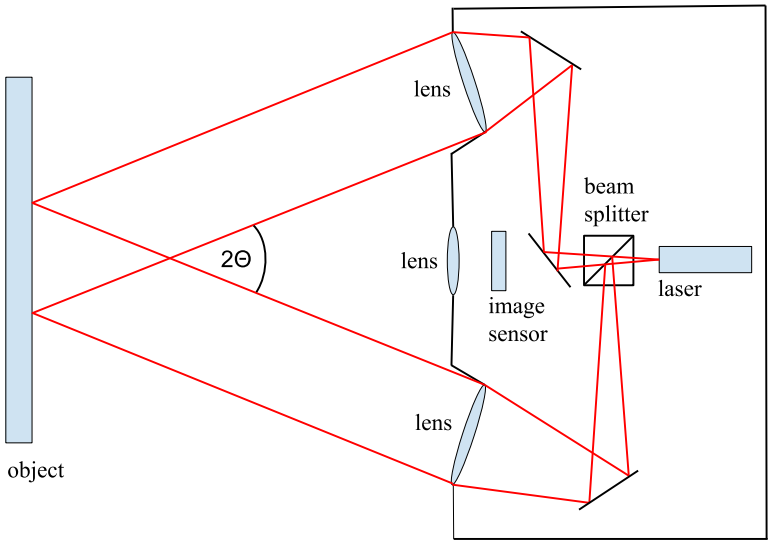

Figure 2.6: Setup of an in-plane sensitive speckle interferometer [12]. Two beams, inclined at equal and opposite angles Θ to the object normal, strike the object. The image is composed of the superposition of two speckle patterns.

measurements [14] on various technical surfaces without the need for artifical markers [15]. These properties make the measurment principle a valuable tool in diverse fields, such as robotic manufacturing [13, 19, 20] and vehicle odometry [21–23]. However, current laser speckle-based in-plane displacement sensors are still limited in their measurement rate, typically operating at rates between 10 and 100 Hz [13, 21].

2.1.2.2 Interferometric setup

This section explores another laser speckle-based measurement principle, based on an interferometric setup, also known as ESPI. Its development can be traced back to the pioneering work of Leendertz [47], with further insights and applications detailed in [11]. In ESPI, two distinct methods are used. For the first method, known as the in-plane sensitive arrangement, the object is illuminated by two beams inclined at equal and opposite angles Θ to the object normal, leading to a superposition of two speckle patterns in the captured image. In the second method, referred to as the out-of-plane sensitive arrangement, a single beam is used to illuminate the object, and the scattered laser light is superpositioned with a smooth reference beam [12]. The setups for these two methods are shown in Figure 2.6 and 2.7, respectively. The main feature of ESPI is displaying correlation fringes resulting from interference effects. To observe these fringes for both arrengentments

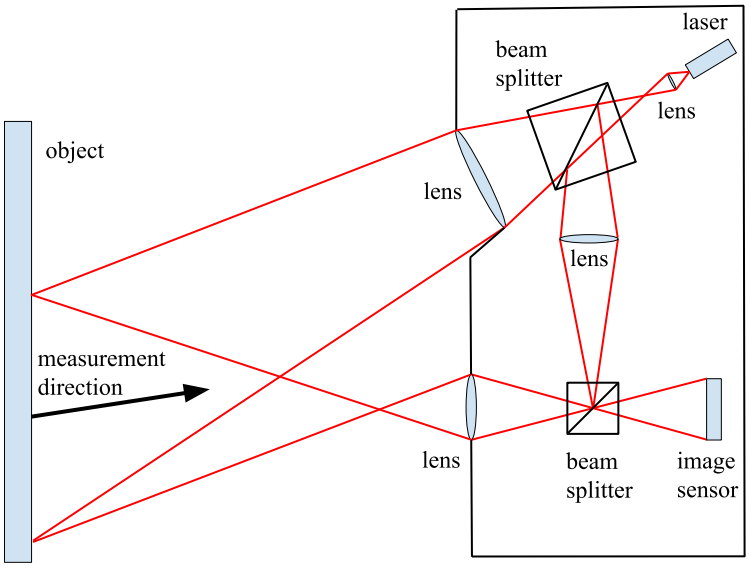

Figure 2.7: Setup of an out-of-plane sensitive speckle interferometer [12]. One beam, inclined at the angle Θ to the object normal, illuminates the object. The reference beam is directly coupled into the camera. The image is composed of the superposition of one speckle pattern and a smooth wavefront.

a reference image before object deformation is saved. The intensity of the reference image can be written as

$$I_R(x,y) = I_1(x,y) + I_2(x,y) + 2\sqrt{I_1(x,y)I_2(x,y)}\cos\phi(x,y) \tag{2.16}$$

where $I_1(x,y)$ is the intensity resulting from beam 1, $I_2(x,y)$ is the intensity resulting from beam 2, $\phi(x,y)$ is the random phase resulting from speckle effects and (x,y) are the spatial cordinates at the image plane. After object deformation, which can result from stretching, compression, shearing, bending or translation, a new image

$$I_D(x,y) = I_1(x,y) + I_2(x,y) + 2\sqrt{I_1(x,y)I_2(x,y)}\cos\Big(\phi(x,y) + \Delta\phi(x,y)\Big) \tag{2.17}$$

is stored, with $\Delta\phi(x,y)$ beeing the phase change due to deformation. Subtraction of the new image $I_D(x,y)$ from the reference image $I_R(x,y)$ is given by

$$\begin{aligned}\Delta I(x,y) &= I_R(x,y) - I_D(x,y)\\ &= 2\sqrt{I_1(x,y)I_2(x,y)}\Big(\cos\phi(x,y) - \cos\Big(\phi(x,y) + \Delta\phi(x,y)\Big)\Big)\\ &= 4\sqrt{I_1(x,y)I_2(x,y)}\sin\left(\phi(x,y) + \frac{\Delta\phi(x,y)}{2}\right)\sin\frac{\Delta\phi(x,y)}{2}\end{aligned} \tag{2.18}$$

where $\sin\left(\phi(x,y)+\Delta\phi(x,y)/2\right)$ is responsible for the high-frequency speckle noise and $\sin(\Delta\phi(x,y)/2)$ represents the low-frequency modulation term, responsible for correlation fringe visibility [12]. Rectifying Equation 2.18 results in the rectified subtraction image

$$|\Delta I(x,y)| = 4\sqrt{I_1(x,y)I_2(x,y)\sin^2\left(\phi(x,y)+\frac{\Delta\phi(x,y)}{2}\right)\sin^2\frac{\Delta\phi(x,y)}{2}}. \quad (2.19)$$

In regions, where the reference image $I_R(x,y)$ and the image after deformation $I_D(x,y)$ are highly correlated, their phase change $\Delta\phi(x,y)$ equals approximately 0 or an integer multiple of 2π, leading to low intensity regions in the rectified subtraction image $|\Delta I(x,y)|$. In uncorrelated areas, regions of higher intensity occur in the rectified subtraction image $|\Delta I(x,y)|$ [11]. With the assumption of in-plane object translation u, the phase change $\Delta\phi(x,y)$ is equal over the whole image coordinates and can be written as

$$\Delta\phi(x,y) = \Delta\phi = \frac{4\pi}{\lambda}u\sin\Theta, \quad (2.20)$$

with λ being the laser wavelength [11]. Therefore, in-plane object translations result in phase changes $\Delta\phi$, which modulate the intensity in the overall rectified subtraction image $|\Delta I(x,y)|$ and not only in regions, compared to general deformations. Figure 2.8a and 2.8b show the rectified subtraction image $|\Delta I(x,y)|$ for phase changes $\Delta\phi$ close to multiple integer values of 2π and for phase changes $\Delta\phi$ of multiple integer values of π, respectively. In Figure 2.9, the relationship between the spatial mean intensity of the rectified subtraction image $|\Delta I(x,y)|$ and the phase change $\Delta\phi$ is shown, while decorrelation effects are neglected for simplicity. Typical fringes with a spacing of 2π are visible.

If general in-plane deformations are to be measured, the phase change $\Delta\phi(x,y)$ becomes unknown and the fringe spacing is not unique anymore. To address this challenge, a different method for calculating the in-plane deformation

$$u_x(x,y) = \Delta\phi(x,y)\frac{\lambda}{4\pi\sin(\Theta)} \quad (2.21)$$

is used [12]. Determining the unknown phase change $\Delta\phi(x,y)$ requires methods of digital phase-shifting interferometry. According to [48] the phase difference between the two interfering beams is deliberately altered in a predetermined way (e.g. with Piezoelectric Transducer (PZT)). Measurements are then taken of the intensity distribution for at least three distinct phase shifts. By knowing the values of these phase shifts, it becomes feasible to compute the initial phase difference between

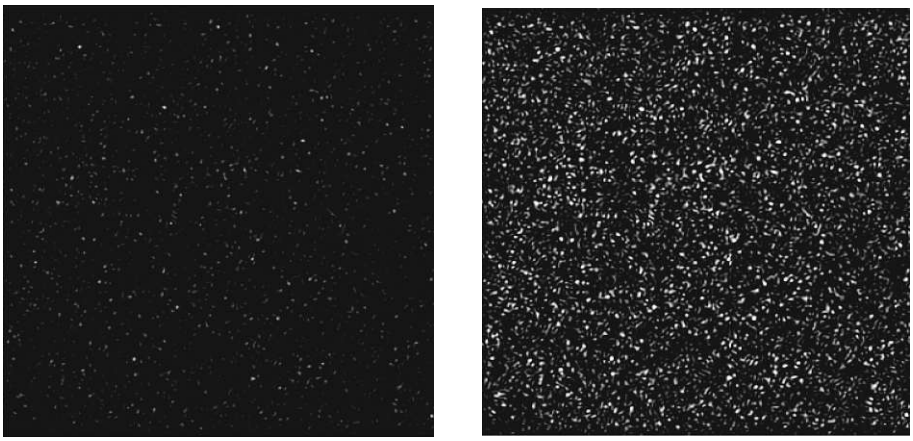

(a) (b)

Figure 2.8: Subtraction images for an in-plane sensitive ESPI setup. (a) Phase changes $\Delta\phi$ close to integer multiples of 2π result in low intensity rectified subtraction images $|\Delta I(x, y)|$. (b) Phase changes $\Delta\phi$ of integer multiples of π result in higher intensity rectified subtraction images $|\Delta I(x, y)|$.

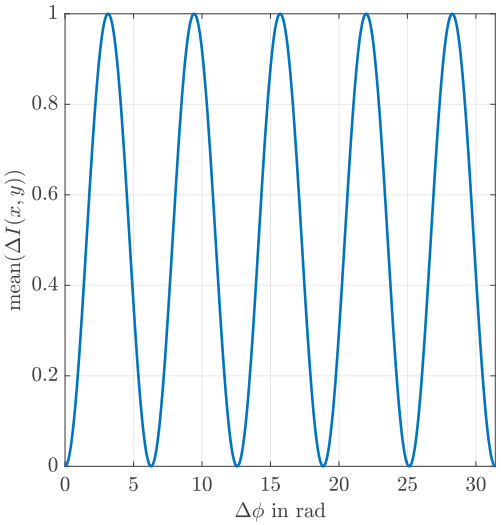

Figure 2.9: Typical correlation fringes due to in-plane translation.

the interfering beams [48]. This approach is also known as the phase-shifting algorithm, with various methods given by the literature [12, 48–50]. Subsequently, the five step algorithm by Kao [50] is described. Before object deformation 5 different phase shifts of -2β, β, 0, β, 2β are introduced between the two interfering beams, resulting in 5 different images $I_a(x,y)$, $I_b(x,y)$, $I_c(x,y)$, $I_d(x,y)$ and $I_e(x,y)$. Setting the tuning parameter β to $\pi/2$ leads to introduced phase shifts ranging from $-\pi$ to π. Therefore, the phase of the speckle pattern for the undeformed object can then be written as

$$\tan\phi(x,y) = \frac{2\Big(I_b(x,y) - I_d(x,y)\Big)}{2I_c(x,y) - I_a(x,y) - I_e(x,y)}. \tag{2.22}$$

Same applies for the images after deformation, leading to $I_a^*(x,y)$, $I_b^*(x,y)$, $I_c^*(x,y)$, $I_d^*(x,y)$ and $I_e^*(x,y)$. The phase of the speckle image after deformation is calculated with

$$\tan\Big(\phi(x,y) + \Delta\phi(x,y)\Big) = \frac{2(I_b^*(x,y) - I_d^*(x,y))}{2I_{Ic}^*(x,y) - I_a^*(x,y) - I_e^*(x,y)}. \tag{2.23}$$

Referring to Equation 2.22 and 2.23 the phase difference is obtained via

$$\Delta\phi(x,y) = \tan^{-1}\left(\frac{2(I_b^* - I_d^*)}{2I_{Ic}^* - I_a^* - I_e^*}\right) - \tan^{-1}\left(\frac{2(I_b - I_d)}{2I_{Ic} - I_a - I_e}\right), \tag{2.24}$$

allowing to calculate the in-plane deformation $u_x(x,y)$ according to Equation 2.21. Typical ESPI setups for measuring in-plane displacement or deformation often employ laser incident angles of around 45 ° or higher [51–53]. While this leads to improved resolutions in the nanometer scale, the setup gets complex and the measurement range is often limited to below 10 μm [12]. In addition to the measurement of in-plane and out-of-plane deformations and displacements, ESPI is also used for vibration analysis, capturing complex geometries, and investigating flow in transparent media [11]. Practical examples are given in [11, 54–57].

2.2 Image processing

The aim of this section is to determine the speckle displacement. For this purpose, a square reference image h_1 with $n_1 \times n_1$ pixel and a square subimage h_2 with $n_2 \times n_2$ pixel are defined. Before the displacement, the subimage has the position (u,v) within the reference image, and after the displacement, it has the position (u_t, v_t). This situation is graphically depicted in Figure 2.10 and is mathematically expressed as

$$h_2(x,y) = h_1(x+u, y+v) + n(x,y), \quad x,y = 1,...,n_2, \quad u,v \in [0,...,n_1-n_2], \tag{2.25}$$

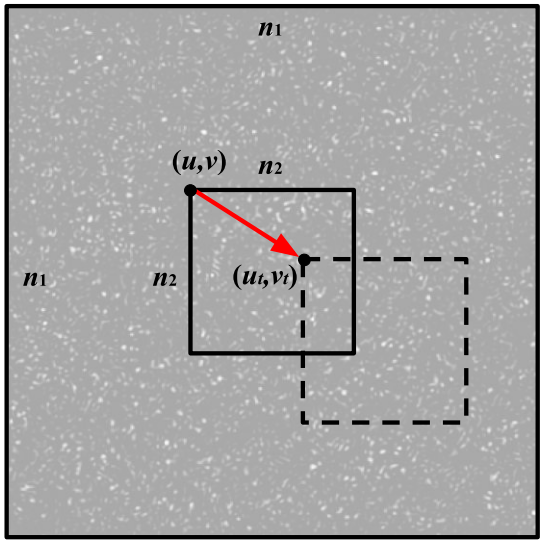

Figure 2.10: Determination of the in-plane object displacement with image processing [59]. The $n_2 \times n_2$ subimage is located at a position (u, v) inside the reference image. After a displacement of d the subimage is located at (u_t, v_t). Using methods to determine the position of the subimage before and after displacement, d can be obtained.

where $n(x, y)$ corresponds to noise due to decorrelation effects [58]. Comparing the position of the subimages before and after the displacement, the displacement can be calculated as

$$d = \sqrt{(u_t - u)^2 + (v_t - v)^2} s_p, \tag{2.26}$$

where s_p is the pixel size. To calculate the displacement, algorithms are required to determine the position of subimages within reference images. Therefore, various methods are described in the subsequent sections.

2.2.1 Feature-based displacement detection

Image matching is a well-established method in computer and machine vision [60]. The initial phase of any matching or recognition algorithm involves identifying points of interest in the images and describing them, also referred to as feature detection and description. There are numerous descriptors available for this purpose, while a comparative analysis of well-established ones such as SIFT, SURF, KAZE, AKAZE, ORB, and BRISK can be found in [61]. After computing the descriptors, a comparison can be made to establish the relationship between images, known as feature matching [60]. Recently, Charrett et al. [62, 63] conducted an examination of the performance and usability of these descriptors for speckle-based systems.

Their publications provide a comprehensive evaluation of widely employed feature detection and matching algorithms, specifically applied to laser speckle patterns for both translation and rotation measurements. In terms of translation measurements, the accuracy achieved through the feature tracking approach was found to be similar to that of correlation-based processing. For in-plane rotation measurements, it was determined that accuracies of less than 0.01 ° can be achieved over an angular range of +/- 10 °. One significant advantage of this method is its capability to measure translations and rotations simultaneously. However, a drawback is the decreasing number of successful matches for larger translations and rotations [62].

2.2.2 Digital Image Correlation in the spatial domain

Referring to Equation 2.25, the speckle shift can be determined by solving an optimization problem. The squared Euclidean distance between the subimage $h_2(x, y)$ and the reference image $h_1(x, y)$, can be defined as the sum of squared differences of the corresponding elements. It works as a measure of similarity and is the starting point for the optimization problem [36, 64]. Minimizing the squared Euclidean distance with the optimization variables u and v is expressed as

$$\min_{u,v} \left(\sum_{x,y} \Big(h_2(x, y) - h_1(x + u, y + v) \Big)^2 \right), \tag{2.27}$$

where the summation over x, y represents the summation over an area of $n_2 \times n_2$ pixel. This can be further expressed as

$$\min_{u,v} \left(\sum_{x,y} \Big(h_2^2(x, y) - 2h_2(x, y)h_1(x + u, y + v) + h_1^2(x + u, y + v) \Big) \right), \tag{2.28}$$

where $h_2^2(x, y)$ is independent of the optimization variables u and v and therefore has no influence on solving the optimization problem. Assuming constant position-independent image energy, the summation term $\sum h_1^2(x + u, y + v)$ becomes independent of the optimization variables u and v as well [64]. Thus, the optimization problem is further simplified, resulting in

$$\min_{u,v} \left(\sum_{x,y} \Big(- h_2(x, y)h_1(x + u, y + v) \Big) \right) = \max_{u,v} \left(\sum_{x,y} \Big(h_2(x, y)h_1(x + u, y + v) \Big) \right). \tag{2.29}$$

The optimization problems described in Equation 2.27 and 2.29 can be solved in the spatial domain using the Sum of Squared Distances (SSD) or Cross Correlation (CC) criteria [59]. In Equation 2.27, the expression within the outer parentheses represents the SSD correlation value

$$C_{SSD}(u, v) = \sum_{x,y} \Big(h_2(x, y) - h_1(x + u, y + v) \Big)^2, \quad x, y = 1, ..., n_2, \tag{2.30}$$

while in Equation 2.29, the expression within the outer parentheses represents the CC correlation value

$$C_{CC}(u,v) = \sum_{x,y} \Big(h_2(x,y) h_1(x+u, y+v) \Big), \quad x,y = 1, ..., n_2, \tag{2.31}$$

for certain indices (u, v). Iterating the indices u and v in Equation 2.30 and 2.31 from 0 to $n_1 - n_2$ spans the correlation matrices C_{CC} and C_{SSD}, respectively. Determining the displacement of the subimage $h_2(x, y)$ within the reference image $h_1(x, y)$ involves either searching the indices of the minimum value within the C_{SSD} matrix for the SSD criteria, or searching the indices of the maximum value within the C_{CC} matrix for the CC criteria. Comparing these two criterias, the CC criteria requires less computational effort, with $n_2^2(n_1-n_2+1)^2$ additions and $n_2^2(n_1-n_2+1)^2$ multiplications [64]. A disadvantage of these methods is that they are not invariant to intensity changes, and determining the right displacement can fail if the reference image energy $\sum h_1^2(x+u, y+v)$ varies with position [64]. Improved correlation criteria, such as the Zero Normalised Sum of Squared Distances (ZNSSD)

$$C_{ZNSSD}(u,v) = \sum_{x,y} \left(\frac{h_2(x,y) - \bar{h_2}}{\sqrt{\sum_{x,y} \left(h_2(x,y) - \bar{h_2} \right)^2}} - \frac{h_1(x+u, y+v) - \bar{h_1}}{\sqrt{\sum_{x,y} \left(h_1(x+u, y+v) - \bar{h_1} \right)^2}} \right)^2 \tag{2.32}$$

and the Zero Normalised Cross Correlation (ZNCC)

$$C_{ZNCC}(u,v) = \frac{\sum_{x,y} \Big(h_2(x,y) - \bar{h_2} \Big) \Big(h_1(x+u, y+v) - \bar{h_1} \Big)}{\sqrt{\sum_{x,y} \left(h_2(x,y) - \bar{h_2} \right)^2 \sum_{x,y} \left(h_1(x+u, y+v) - \bar{h_1} \right)^2}} \tag{2.33}$$

criteria overcome this limitation by normalizing the images [59, 64]. This normalization results in more accurate correlation criterias, that are robust against variations in offset and linear scale caused by illumination changes [59]. The values of a typical ZNCC correlation matrix for speckle images are displayed in Figure 2.11. It shows a distinct peak, surrounded by noise. Although ZNCC and ZNSSD criteria are more accurate in determining the displacement, their computational effort significantly rises.

2.2.3 Digital Image Correlation in the frequency domain

Another method of solving the optimization problem described in Equation 2.29 involves employing Fourier Transformation to the reference image h_1 and subimage h_2 and solving the problem in the frequency domain [36, 58, 64, 65]. This method requires zero-padding of both the reference image h_1 and the subimage h_2 to sizes

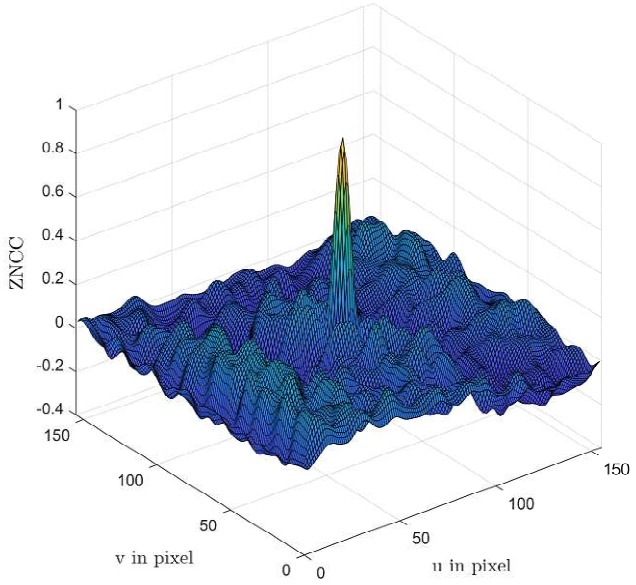

Figure 2.11: ZNCC correlation between a subimage and a reference image. A distinct peak, representing a strong correlation between the two images, is visible at indices $(u, v) = (80{,}78)$.

of $m \times m$, where $m = n_1 + n_2$ [65]. The two-dimensional discrete Fourier transform of the reference image h_1 and subimage h_2 can be written as

$$H_1(r,s) = \frac{1}{m^2}\left(\sum_{u=0}^{m-1}\sum_{v=0}^{m-1}(h_1(u,v)e^{-2\pi i(ru+sv)/m})\right) \tag{2.34}$$

and

$$H_2(r,s) = \frac{1}{m^2}\left(\sum_{u=0}^{m-1}\sum_{v=0}^{m-1}(h_2(u,v)e^{-2\pi i(ru+sv)/m})\right) \tag{2.35}$$

with (r, s) beeing the spectral domain coordinates. With Inverse Fourier Transformation of the elementwise multiplication of H_2^* and H_1, the optimization problem can be written as

$$\max_{u,v}\left(\mathcal{F}^{-1}(H_2^* H_1)\right), \tag{2.36}$$

where * represents the conjugate complex of the matrix elements. The Inverse Fourier Transformation converts the spectral domain coordinates (r, s), back to the spatial coordinates (u, v). Fourier Transformations are efficiently executed using the Fast Fourier Transformation (FFT) [65]. Solving the optimization problem in the frequency domain with FFT involves $12n_1^2 \log_2 n_1$ real multiplications and

$18n_1^2 \log_2 n_1$ real additions/subtractions [64]. In contrast, the CC criteria, which solves the optimization problem in the spatial domain, requires $n_2^2(n_1 - n_2 + 1)^2$ additions and $n_2^2(n_1 - n_2 + 1)^2$, as mentioned in Section 2.2.2. When the reference image size n_1 is much larger than the subimage size n_2, solving in the spatial domain is more efficient. Conversely, when the subimage size n_2 approaches the reference image size n_1, particular for large image sizes, solving in the frequency domain becomes more efficient [64].

2.2.4 Achieving subpixel resolution

The previously described DIC methods from Sections 2.2.2 and 2.2.3 can detect displacements with a resolution of the pixel size of the image sensor. However, this is far from the required measurement resolution in many real applications [32]. To further improve the resolution and accuracy of DIC, different subpixel registration algorithms have been developed, such as intensity interpolation, correlation curve fitting, Newton Raphson iteration, gradient-base methods, double Fourier transform, cross-search, gentic algorithms and even artificial neural network methods [32–34]. Due to their accuracy up to 0.01 pixel, the correlation curve-fitting method and gradient-based method belong to the most commonly used algorithms in DIC [32]. Below, these methods are described based on the work of Bing et al [32]. The curve-fitting method is based on a quadratic approximation of the correlation matrix around the maximum correlation value

$$C(u, v) = a_0 + a_1 u + a_2 v + a_3 u^2 + a_4 uv + a_5 v^2. \tag{2.37}$$

With known parameters a_1, a_2, a_3, a_4, and a_5, the index position (u^*, v^*) of the maximum correlation value can be found by taking the derivatives of Equation 2.37 with respect to u and v, and setting them to zero. Solving the resulting equation system yields in the index position with subpixel accuracy

$$u_* = \frac{2a_1 a_5 - a_2 a_4}{a_4^2 - 4a_3 a_5} \tag{2.38}$$

and

$$v_* = \frac{2a_2 a_3 - a_1 a_4}{a_4^2 - 4a_3 a_5}. \tag{2.39}$$

In comparision to the correlation curve fitting approach, gradient-based methods utilize a different approach to achieve subpixel accuracy. Therefore, Equation 2.25, which describes searching the subimage $h_2(x, y)$ within the reference image $h_1(x, y)$ is modified to

$$h_2(x, y) = h_1(x + u + \Delta x, y + v + \Delta y), \quad x, y = 1, ..., n_2, \quad u, v \in [0, ..., n_1 - n_2], \tag{2.40}$$

where Δx and Δy represent the subpixel displacements. A first-order Taylor series expansion of h_1, neglecting higher-order terms, can be written as

$$h_1(x+u+\Delta x, y+v+\Delta y) = h_1(x+u, y+v)+\Delta x h_{1,x}(x+u, y+v)+\Delta y h_{1,y}(x+u, y+v), \tag{2.41}$$

where $h_{1,x}$ and $h_{1,y}$ are the first-order spatial derivatives of the reference image intensities. Further, solving Equation 2.41 with least squares leading to the equation system for the subpixel displacements

$$\begin{bmatrix}\Delta x\\ \Delta y\end{bmatrix} = \begin{bmatrix}\sum_{x,y}(h_{1,x})^2 & \sum_{x,y}(h_{1,x}h_{1,y})\\ \sum_{x,y}(h_{1,x}h_{1,y}) & \sum_{x,y}(h_{1,y})^2\end{bmatrix}^2 \cdot \begin{bmatrix}\sum_{x,y}\Big((h_2-h_1)h_{1,x}\Big)\\ \sum_{x,y}\Big((h_2-h_1)h_{1,y}\Big)\end{bmatrix} \tag{2.42}$$

Both correlation curve-fitting and gradient-based methods offer subpixel accuracies up to 0.01 pixel, making them suitable for high-precision displacement measurements. However, these approaches are relatively slow, often taking several seconds to compute [32]. This makes them unsuitable for applications where minimal latency is required. In such cases, simpler methods like linear intensity interpolation are required.

2.3 Methods to extend the measurement range

Referring to Section 2.1.2.1, the measurement range of laser speckle-based displacement sensors is limited due to decorrelation effects. In recent years different methods, such as resetting of the reference image [19], dual wavelength correlation [14] and an compensation based approach [13], have been developed to address this challenge. In this Section the mentioned methods are further described.

2.3.1 Resetting of the reference image

In cases where in-plane object displacements exceed the area covered by the reference image, detecting an overlap between the subimage and the reference image becomes impossible. Therefore, it is advisable to capture a new reference image either when the subimage reaches the edge of the reference image or when significant decorrelation is observed [19]. Each re-referencing operation introduces a measurement error, depending mainly on the resolution of the sensor and uncertainty due to decorrelation. With multiple re-referencing operations, necessary for significantly extending the measurement range of speckle-based in-plane displacment sensors, these errors accumulate, resulting in increased measurement uncertainty. The increased uncertainty is confirmed by measurements conducted in [66], where researchers applied this methodology to measure the in-plane translation of an industrial robot over a travel distance of 0.5 m, yielding a measurement

error of approximately 130 μm. While this approach offers the advantage of easy implementation it has the drawback of increased uncertainty.

2.3.2 Dual wavelength correlation

Another approach for extending the measurement range of speckle based in-plane displacement sensors is based on resetting the reference image in a dual wavelength correlation setup, presented in [14]. Unlike the approach in Section 2.3.1, which relies on re-referencing in the case of significant decorrelation, the dual-wavelength correlation method resets the reference image at the highest correlation value, ensuring less measurement uncertainty. However, a limitation of this method is its ability to measure in-plane displacements in only one DoF. Figure 2.12 shows the dual wavelength based setup, where collimated green and red laser beams illuminate an optically rough object. The two laser spots have identical diameters but different wavelengths. They are separated with a small position offset to create an overlapping area on the object. The green and red speckle images are captured with a color image sensor, which allows distinguishing between them. The key principle of the dual wavelength correlation method is to achieve a high correlation between the red and green speckle pattern [14]. Therefore, small wavelength separation, large speckle size, and precise alignment is suggested [14]. Before object displacements, the red and green reference images are stored as red-0 and green-0, respectively. Figure 2.13 shows the ZNCC for different object displacements in the displacement direction. The green curve represents the correlation between the green reference image green-0 and the actual image green-i. The red curve represents the correlation between the red reference image red-0 and the actual green image green-i. If the object displacement equals the position offset between the laser beams, the green laser beam illuminates the same position as the red beam did for the reference image. This results in maximum correlation between green-i and red-0, and the two reference images can be resetted with minimal error [14]. The limit for errors is now only the spatial resolution of the system, while the additional uncertainty due to decorrelation is eliminated.

2.3.3 Compensation-based measurement configuration

To overcome decorrelation effects, a compensation-based laser speckle sensor system, as shown in Figure 2.14, can be utilized. The system consits of a laser, an image sensor, an aperture and two linear stages, which actively track the in- and out-of-plane motion of the object via feedback control. This ensures that the relative in- and out-of plane displacement between the object and the sensor remains zero, thereby preventing decorrelation. A comprehensive explanation and performance evaluation of the method is given in [13]. The author demonstrates a small spatial

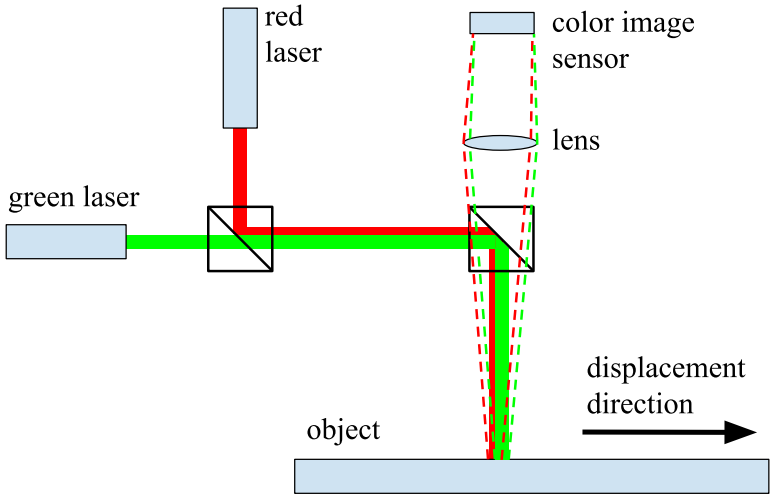

Figure 2.12: Setup for dual wavelength correlation [14]. An optically rough object is illuminated by a red and green laser. The two spots have the same size and an overlapping area on the object. The image is captured with a color image sensor to distinguish between the red and green speckle pattern.

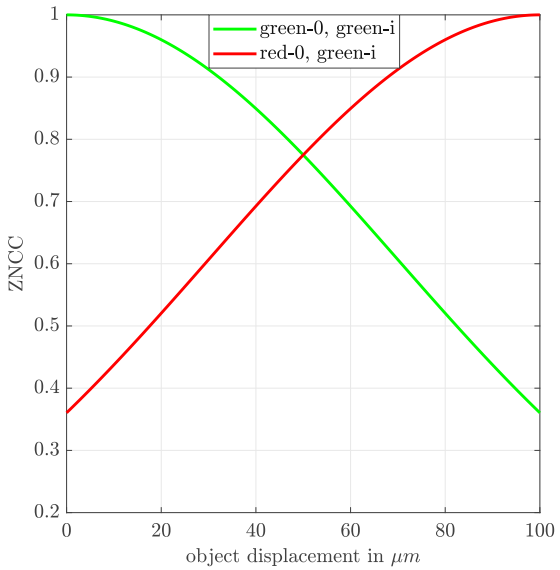

Figure 2.13: ZNCC in a dual wavelength correlation setup. Object displacements in the displacment direction rising correlation between the red reference image red-0 and the actual green subimage green-i. The correlation between the green reference image green-0 and the actual green image green-i decreases.

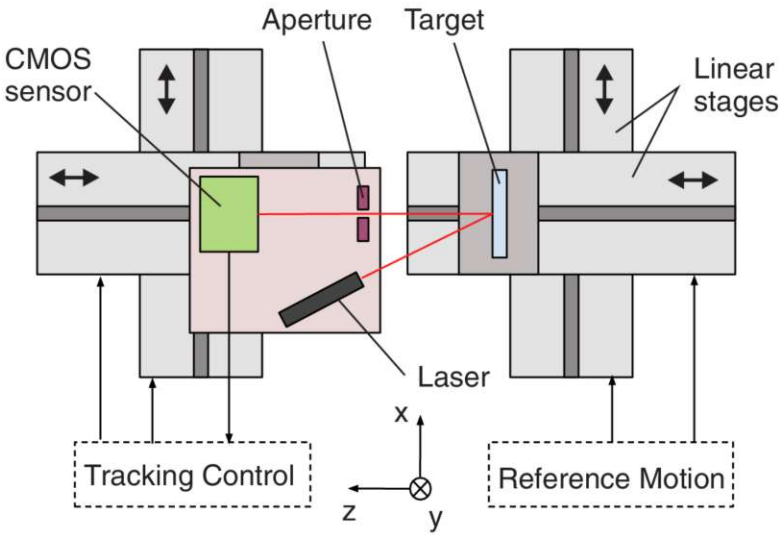

Figure 2.14: Setup for compensation based speckle sensing [13]. An optically rough object is illuminated by a laser. Inserting an aperture in the optical path enables the measurment of in- and out-of plane displacements simultaneously. Via feedback control the position of the object is tracked, which results in high correlation over the whole measurment range.

root mean square tracking error, ranging from 8.75 to 13.25 μm, for different 2D trajectories within a 1×1 mm area. Despite maintaining high correlation throughout the entire measurement range, the existing measurment system comes with two drawbacks. First, it has a more complex setup due to the necessity for tracking stages. Second, it operates at a measurement rate of 10 Hz, which is too low for real-world applications [13]. This clearly underscores the need for further research.

2.4 Research questions

Existing methods for measuring in-plane displacements encounter various drawbacks. Interferometric principles offer high resolution but are limited in their measurement range and have complex setups. Marker-based principles, on the other hand, may not always be feasible, particularly for inline metrology applications where high throughput is desired and applying markers to every object is impractical. Laser speckle-based methods demonstrate significant potential, especially with advancements in achieving subpixel resolution and extending the measurement range present in the literature. Consequently, laser-speckle-based in-plane displacement sensors offer a simple setup, high resolution, an expandable measurement range and eliminate the need for additional markers. However, challenges remain in improving

the measurement rate, with the bottleneck often being the computational effort in image processing. This leads to the formulation of the first research question of this thesis.

Research Question 1

Is it possible to design and build a laser speckle-based in-plane displacement sensor, which is capable of measuring with a resolution in the single micrometer range and measurement rates up to several 10kHz?

In pursuit of achieving subpixel resolution, methods such as correlation curve fitting, Newton-Raphson, and gradient-based methods, are considered optimal according to their accuracy. However, these methods require solving equation systems, making them non-real-time capable and leading to increased latency. This conflicts with the aim of achieving high measurement rates. Simpler methods like linear intensity interpolation, while unable to match the resolution provided by the aforementioned techniques, can be implemented easily and, importantly, in real-time with lower latency. This raises the second research question.

Research Question 2

Can the resolution of the sensor be increased with subpixel interpolation methods without decreasing the measurement rate?

CHAPTER 3

Simulation and Design

Before the prototype is built, several geometric considerations are taken into account. The goal is to achieve maximum sensitivity for measuring in-plane displacements with minimal crosstalk. Furthermore, simulations are conducted to validate theory and to acquire methods, which further optimize the sensor's measurement rate. Based on the results, requirements can be specified, from which the corresponding components are then selected, and the prototype is constructed.

3.1 Setup geometry

The prototype is based on an OLSP setup to ensure a compact sensor design. This offers the advantage of easy sensor integration into various systems and eliminates the need for additional lenses. Considering the design of a sensor prototype to measure in-plane displacements, strains and rotations can be neglected. Taking this assumption into account, target displacements a_x, a_y, and a_z in the object plane lead to speckle shifts

$$\begin{aligned} A_\zeta = &- a_x \left(\frac{L_o}{L_s}(l_{sx}^2 - 1) + l_x^2 - 1 \right) - a_y \left(\frac{L_o}{L_s} l_{sx} l_{sy} + l_x l_y \right) \\ &- a_z \left(\frac{L_o}{L_s} l_{sx} l_{sz} + l_x l_z \right) = k_x a_x + k_{xy} a_y + k_{xz} a_z \end{aligned} \tag{3.1}$$

and

$$\begin{aligned} A_\eta = &- a_x \left(\frac{L_o}{L_s} l_{sy} l_{sx} + l_y l_x \right) - a_y \left(\frac{L_o}{L_s} (l_{sy}^2 - 1) + l_y^2 - 1 \right) \\ &- a_z \left(\frac{L_o}{L_s} l_{sy} l_{sz} + l_y l_z \right) = k_{yx} a_x + k_y a_y + k_{yz} a_z \end{aligned} \tag{3.2}$$

in the image plane [45], as illustrated in Figure 2.5. The sensitivity parameters of the senor are represented by k_x and k_y, while k_{xy}, k_{xz}, k_{yx} and k_{yz} represent the undesired crosstalk. To maximize sensitivity and minimize crosstalk, the image plane and object plane are aligned in parallel, with their origins situated along a connecting line perpendicular to the planes. According to Equation 3.1 and 3.2, the laser is best placed along that connecting line. However, this is not possible as the laser has to be placed in front of or behind the image sensor. Consequently, the laser needs to be shifted towards the x- or y-direction and tilted by a small angle θ relative to the object normal. Using $l = (0, 0, 1)^T$ and $l_s = (l_{sx}, 0, l_{sz})^T = (\sin(\theta), 0, \cos(\theta))^T$, Equation 3.1 and 3.2 can be written as

$$\begin{aligned} A_\zeta &= a_x \left(1 + \frac{L_o}{L_s} (1 - l_{sx}^2) \right) + a_z \left(-\frac{L_o}{L_s} l_{sx} l_{sz} \right) \\ &= a_x \left(1 + \frac{L_o}{L_s} \cos(\theta)^2 \right) + a_z \left(-\frac{L_o}{2L_s} \sin(2\theta) \right) \\ &= k_x a_x + k_{xz} a_z \end{aligned} \tag{3.3}$$

and

$$A_\eta = a_y \left(1 + \frac{L_o}{L_s} \right) = k_y a_y. \tag{3.4}$$

Through the selection of above design parameters the crosstalk parameters k_{xy}, k_{yx} and k_{yz} have become 0 in Equation 3.3 and 3.4. Only the crosstalk parameter k_{xz} between x- and z-axis remains relevant. Considering perfect collimated illumination, the radius of curvature at the target L_s can be set to ∞ [67], leading to the in-plane sensitivities $k_x = 1$ and $k_y = 1$, and no crosstalk k_{xz}. Due to this, the speckle shifts A_ζ and A_η in the image plane are equal to the object displacements a_x and a_y in the object plane. Such an setup leads to the highest sensitivity for an OLSP measurement system with no crosstalk. By inserting a lens between the laser and the object, and thereby adjusting the radius of curvature L_s, the sensitivity can further be increased [68]. In this case, however, crosstalk can no longer be neglected.

3.2 Simulation

In [46], the implementation of a simulation framework for the design of optical sensor assemblies capable of handling both OLSP and SLSP effects is shown. The

idea is to simulate the laser spot on the target by multiple point sources. Each point source is further approximated by multiple rays. Via ray tracing algorithms, the rays of every point source are traced to the image sensor, as shown in Figure 3.1a. Using the known optical path lengths, a phase and intensity image for every point source can be calculated. The speckle image is created by superposition over all complex images. To simulate in-plane object displacements, the locations of the point sources are shifted accordingly. The resulting speckle shifts are identified by calculating the correlation between a reference and every subsequent subimage. A detailed explanation of the algorithm is given in [46].

The simulation framework is implemented in MATLAB (The MathWorks Inc., Natick, Massachusetts, USA) with a laser diameter D of 3 mm, a laser wavelenght λ of 640 nm, a radius of curvature L_s of ∞, a detector to object distance L_o of 100 mm and a laser incidence angle θ of 10 ° realtive to the object normal. The parameters are chosen based on simulating a compact setup with zero crosstalk. Reffering to Equation 2.11, a speckle size s_{sp} of 26.03 μm or 3,72 pixel is expected. The laser spot on the target is approximated by 500 point sources with 1500 rays each. For image processing the used correlation algorithm is *normxcorr2*, which is implemented by the Image Processing Toolbox. Figure 3.1b shows the speckle image, consisting of 400 x 400 pixel, with a pixel size of 7 x 7 μm. To minimize computational effort, a 50 x 50 pixel window and a 1 x 50 pixel window, as shown in Figure 3.1b and 3.1c, are defined. The simulation of object displacements in x-direction is performed for 29 positions over a range of 196 μm, with a step size of 7 μm. The reference image is taken at center location. According to Figure 3.2a, the calculated speckle shift equals the object position for the 50 x 50 pixel window over the whole in-plane translation range. For the 1 x 50 pixel window a error of 7 μm occurs at object positions -91 μm and -98 μm. This is because the correlation decreases more rapidly for the 1 x 50 pixel window compared to the 50 x 50 pixel window, as visible in Figure 3.2b. The disadvantage of using a 1 x 50 pixel window is the faster decorrelation and the loss of the second DoF. Due to faster decorrelation signals are lost in noise earlier, leading to a smaller measurement range for the 1D pixel window, compared to the 2D pixel value. Since there are multiple methods to increase the range of motion (compensation based approach [13], resetting the reference image [19], dual-wavelength correlation [14]), the disadvantage of faster decorrelation can be neglected. A significant advantage of using the 1 x 50 pixel window is, that a line sensor is sufficient, and no 2D image sensor is required, allowing higher frame rates [69, 70] and less computational effort.

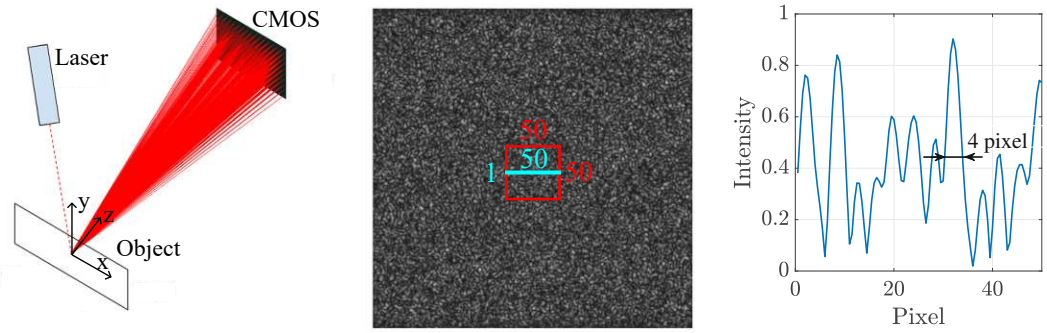

Figure 3.1: Simulation framework for the design of OLSP setups. (a) Ray tracing for a single point source, which is approximated by N rays towards the detector. (b) Simulated 400 x 400 pixel speckle image with user definded windows of interest. (c) 1D pixel window with a speckle size s_{sp} of approximately 4 pixel.

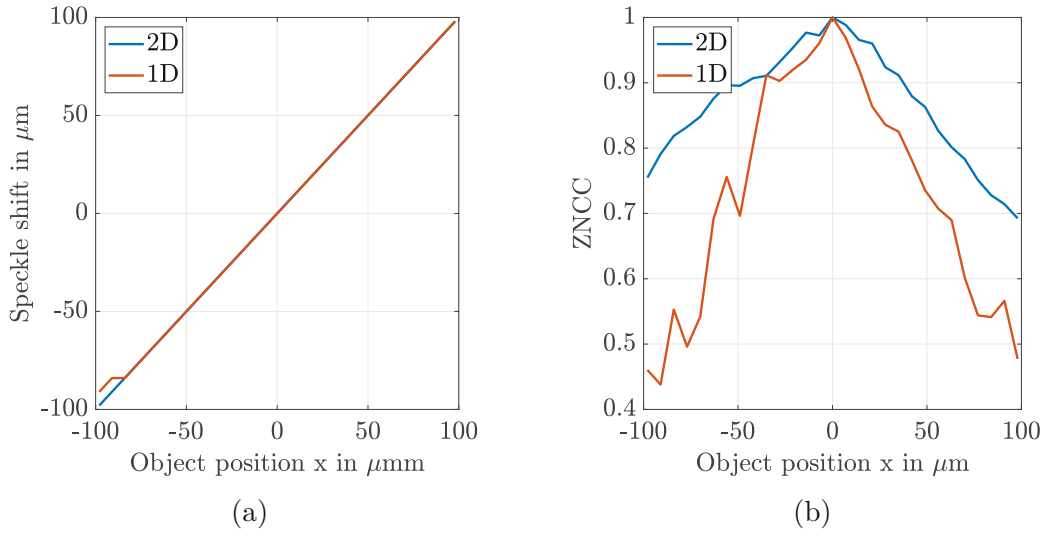

Figure 3.2: Simulation output for object displacement in x-direction for a 50 x 50 pixel window (blue) compared to a 1 x 50 pixel window (red). (a) Calculated speckle shift in μm. The speckle shift matches the object displacment for the 2D pixel window over the entire in-plane translation range of 200 μm. For the 1D correlation window small deviations at object translations below -91 μm can be seen. (b) Calculated zero normalized cross correlation. As expected, the 1D pixel window decorrelates more rapidly.

3.3 Requirements

To build a sensor prototype, a laser, an image sensor, and real-time capable communication and processing hardware, such as an /acrfullFPGA or microcontroller, are required. Referring to the design considerations from Section 3.1 the laser has to be collimated to avoid the need of additional collimation lenses. A narrow spectrum of emitted light is beneficial for speckle images with a good signal-to-noise ratio. In order to achieve sufficient contrast, a spectrum narrower than 1 nm is required [71]. As mentioned in Section 2.4, the question arises whether it is possible to measure in-plane displacements with a resolution in the single micrometer range and measurement rates of up to several 10 kHz. Therefore, the image sensor requires a pixel size in the single μm range or lower and a minimum frame rate of 10 kfps. The resolution of the prototype is determined by the pixel size, and can be further improved by subpixel interpolation. While the usage of 2D image sensors is possible, line sensors are preferred due to their higher frame rates and less computational effort for pixel processing. In addition, CMOS technology is of advantage to be used as the sensor type, since they are more suitable for high-speed applications than Charge-Coupled Device (CCD) sensors [72]. For image readout and pixel processing, a communication and processing hardware is necessary. It has to be compatible with the line sensor, which means that it must have sufficient General Purpose Inputs Outputs (GPIOs) for reading out the whole line sensor, and its oscillator frequency should be at least equal to the maximum allowed input clock frequency of the line sensor. The prototype further requires an interface board to connect the communication and processing hardware with the image sensor, as well as a housing. The overall size of the sensor prototype should be kept small in order to ensure compactness. Figure 3.3 visualizes the interfaces between the individual components through a block diagram. In addition to the sensor prototype, a power supply, and a personal computer for FPGA programming are depicted. Table 3.1 presents a summary of the requirements.

3.4 Specification

With the defined requirements from Table 3.1 the goal is to chose components, which fulfill all the requirements. The following sections summarize the key information about the selected components and clarify why they are chosen and why they are designed in this particular manner.

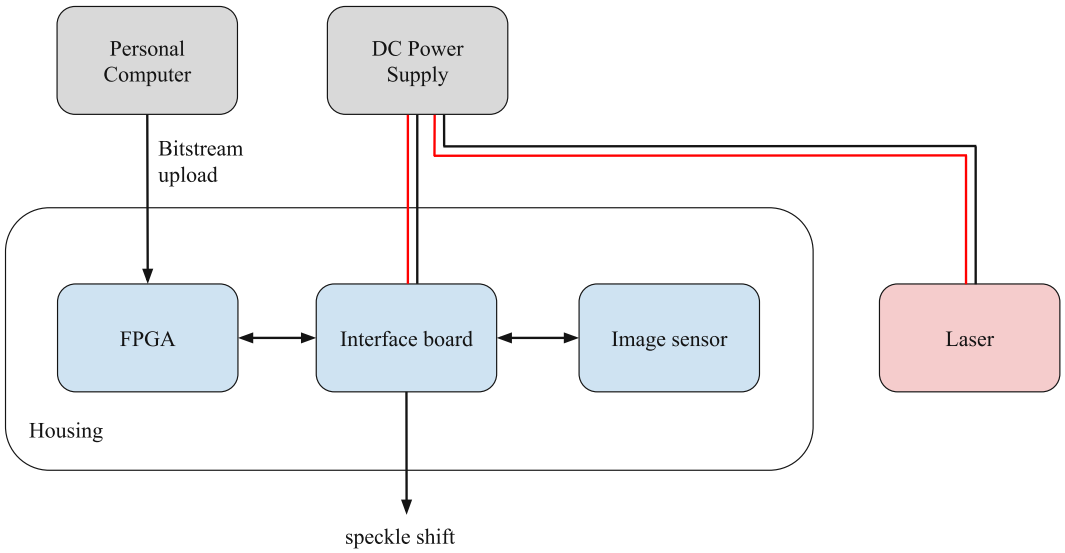

Figure 3.3: Block diagram of the sensor prototype. The FPGA communicates with the image sensor over an interface board. The programming and bitstream upload of the FPGA is done using a personal computer. A DC power supply provides the voltage levels for the individual components. The measured speckle shift can be read from the interface board.

Table 3.1: Requirements for the sensor prototype and its components. The laser requirements allow for speckle imagse with good contrast. The requirements for the image sensor are derived regarding resolution and measurement rate. The FPGA must be compatible with the image sensor.

Laser	spectral width	less than 1 nm
	collimation required	yes
Image sensor	type	CMOS line sensor
	pixel size	single μm or below
	frame rate	higher than 10 kfps
communication hardware	number of GPIOs	depends on image sensor
	oscillator frequeny	depends on image sensor
Prototype	size	compact

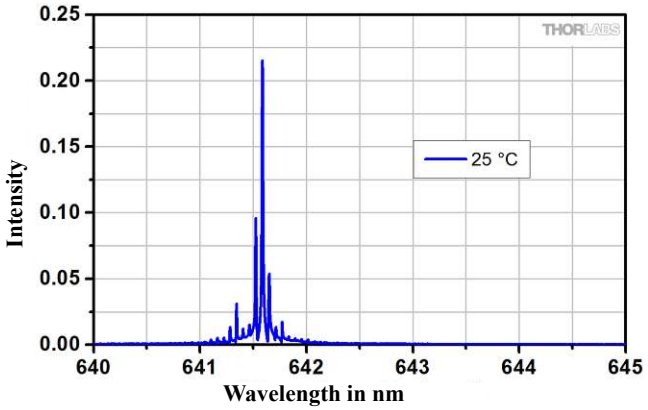

Figure 3.4: Typical spectrum of PL204 [73]. The intensity peaks are between 641 and 642 nm, with a standard deviation $\sigma < 0.5$ nm. The narrow spectrum ensures a speckle image with sufficient contrast [71].

3.4.1 Laser

The PL204 laser (Thorlabs Inc., Newton, New Jersey, USA) is a compact, collimated class 2 laser diode module that produces an output beam with a circularized beam shape. All of its properties originate from [73]. It has a typical output power of 0.9 mW and a narrow spectrum around the wavenlength of approximately 641.5 nm, as shown in Figure 3.4. The housing is 60.2 mm long with a diameter of 11 mm, which offers the ability of easy integration into various systems. It fulfills the compactness, collimation and narrow spectrum requirements from Table 3.1 and is therefore suitable for the sensor prototype.

3.4.2 Image sensor

The DR-B&W-4K-7-Invar CMOS sensor (ams-OSRAM AG, Premstätten, Styria, Austria), as shown in Figure 3.5a, is composed of two monochrome line sensor segments, each with 2080 pixels, arranged side by side. All of its specifications are derived from [74]. It features a pixel size of 7 x 7 μm and line rates up to 80 klines/s. Each pixel includes an on-pixel Analog Digital Converter (ADC) with a resolution up to 13 bit. The configuration of the line sensor is performed through an SPI interface. The maximum input clock frequency is the ADC clock, with up to 100 MHz, the pixel and SPI clocks need to be lower. The output interface is digital parallel, which means that with every clock cycle, the sensor transmits 4 pixel values over 52 pins (4 x 13 bit) for the case of maximum ADC resolution. As the readout for each segment is completely independent, this is equivalent to the sensor transmitting 2 pixel values over 26 pins every clock cycle per segment.

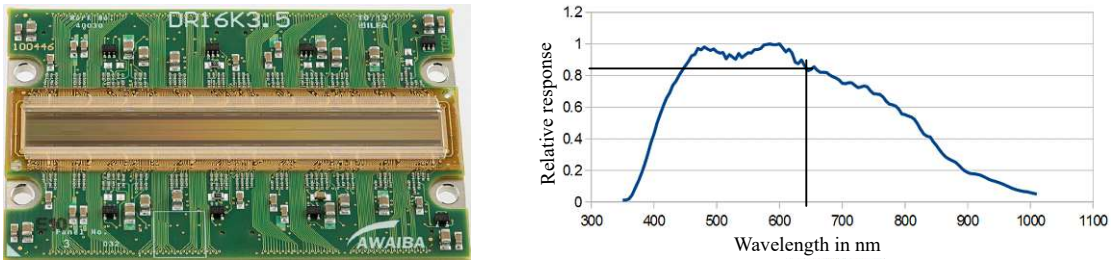

(a) (b)

Figure 3.5: Dragster line sensor [74]. (a) Dragster board with mounted CMOS line sensor and external components. (b) Relative spectral response. For the chosen laser wavelength, the sensitivity of the CMOS line sensor is approximately 0.85.

The sensor has a 120 pin pinout using a Molex 055339-1208 connector. 71 pins are digital inputs and outputs, while the remaining ones are used for analog-, digital-, and Electrostatic Discharge (ESD)-voltage supply. The physical dimensions of the line sensor are 35 x 32.5 x 4.94 mm. Referring to Figure 3.5b, the sensitivity at the laser wavelength of 641.5 nm is approximately 0.85, rendering the line sensor compatible with the chosen laser. Moreover, the line sensor meets the compactness, pixel size, and frame rate requirements outlined in Table 3.1.

3.4.3 FPGA

As shown in Figure 3.3 the FPGA has to communicate with the line sensor over the interface board to capture images and process the pixel values. The calculated shift is output over the interface board. The preferred output interface for the shift is over N digital pins, with N being at least 8. This offers a measured shift range from

$$d_{min} = -2^7 \frac{s_p}{q} \tag{3.5}$$

to

$$d_{max} = (2^7 - 1) \frac{s_p}{q} \tag{3.6}$$

where s_p is the pixel size and q the subpixel interpolation factor. Setting the pixel size s_p to 7 μm and assuming a maximum interpolation factor of 4 results in a d_{min} of -224 μm and a d_{max} of 222.25 μm. The useage of a digital parallel interface eliminates the impact of noise on one hand and minimize latency on the other, as the speckle shift becomes immediately visible at the output following the pixel processing. For image capturing, there is a tradeoff between the chosen resolution and the line rate, as ADC conversion takes longer for higher resolutions. The prototype shall be capable of reading out the line sensor with the highest resolution,

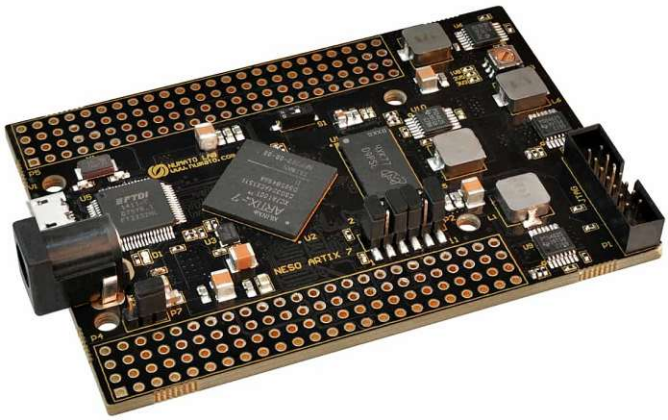

Figure 3.6: Neso Artix 7 FPGA development board [75]. It comprises a 100 MHz oscillator and two 24 x 4 pinheader, from which 140 can be used as GPIOs. The bitstream upload is possible via USB.

if needed. Therefore, the usage of all 71 GPIOs of the line sensor is required. This leads to the summarized requirements for the FPGA: At least 79 GPIOs (71 + 8) are needed, and the clock frequency must be greater than or equal to the maximum allowed input clock of the line sensor of 100 MHz. Figure 3.6 shows the Neso Artix 7 FPGA development board (Numato Systems Pvt Ltd., Hulimangala, Karnataka, India). All of its specifications are derived from [75]. It has 140 GPIOs and a 100MHz oscillator, making it suitable for the sensor prototype. The board dimensions are 83.8 x 57.53 x 16 mm. Further decreasing the size would require designing a custom FPGA board (e.g. with the Artix 7), which is not in the scope of this thesis. However, it should be kept in mind for future work.

3.4.4 Interface board

The interface board serves three functions. Firstly, it supplies the voltages to the line sensor. Secondly, it connects the pins from the line sensor to the GPIOs of the FPGA development board, as visualized in Figure 3.3. Lastly, it provides a pin header for the measured speckle shift. Figure 3.7 illustrates the PCB, designed in EAGLE (Autodesk Inc., San Rafael, California, USA). The red box involves a 5 V power supply through banana jacks. Following that, three voltage regulators, represented by the violet box, are set to 3.3 V, providing for the line sensor's analog, digital, and ESD voltage requirements [74]. Pin headers, shown as blue boxes, are positioned on both the top and bottom of the PCB, facilitating easy connection between the hardware interface and the FPGA board. This is achieved by stacking them together through a male and female pinout. The connection to the line sensor is made via a 120-pin Molex 055339-1208 connector, highlighted by the green box.

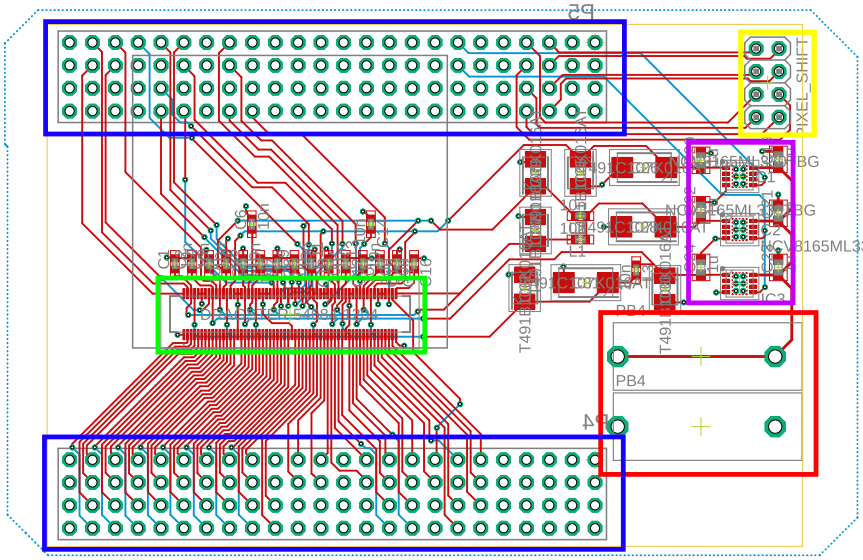

Figure 3.7: PCB of the hardware interface. It has 3 voltage regulators (violate) for supplying the line sensor. The connection to the FPGA and line sensor is done over pinheaders (blue) and a Molex 055339-1208 connector (green). The calculated shift is provided over a 8 pin digital interface (yellow).

On the bottom of the connector, there are mainly data traces, while on the top, there are mainly supply voltages or ground connections. For this reason, there are many smoothing capacitors located close to the top pins of the connector. The output interface, represented by the yellow box, is placed in the top right corner. The board with its components has a physical size of 83.8 x 57.53 x 18.5 mm. The length and width are chosen to be the same as for the FPGA board since they are stacked together.

3.4.5 Prototype

Figure 3.8 shows the FPGA, interface board, and line sensor stacked together. The FPGA is positioned beneath the interface board, while the line sensor is placed on top of it. The line sensor is mounted on a small metal plate, which back is covered with insulating tape to prevent short circuits. The wires at the bottom of Figure 3.8 serve for debugging purposes and laser alignment. They include signals of the SPI interface, signals necessary for triggering the image capture, and signals representing pixel values. In Figure 3.9, the sensor prototype is displayed inside its housing. Compared to Figure 3.8 it is visualized upside down. The housing is designed using SolidWorks (Dassault Systémes S.A., Vélizy-Villacoublay, France)

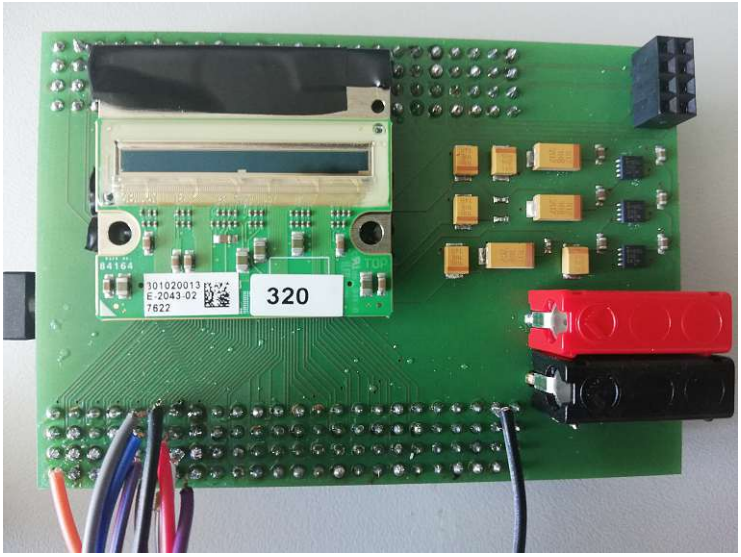

Figure 3.8: Sensor prototype. The FPGA, hardware interface and line sensor are stacked together. The FPGA is placed under the hardware interface, the line sensor is placed on top of it. The additional wires are for debugging purposes.

and manufactured through 3D printing. It provides a secure enclosure for the prototype, preventing measurement errors caused by slipping. The simple and compact design allows integration into various systems. The overall prototype has physical dimensions of 96 x 70 x 40 mm. With the chosen components the requirements outlined in Table 3.1 are fullfilled. An overview of the componet specifications is given in Table 3.2.

Table 3.2: Specifications of the sensor prototype and its components.

Laser	spectral width	< 0.5 nm
	collimation	yes
Image sensor	type	CMOS line sensor
	pixel size	7 μm
	frame rate	up to 80 klines/s
FPGA	number of GPIOs	140
	oscillator frequeny	100 MHz
Prototype	size	96 x 40 x 70 mm

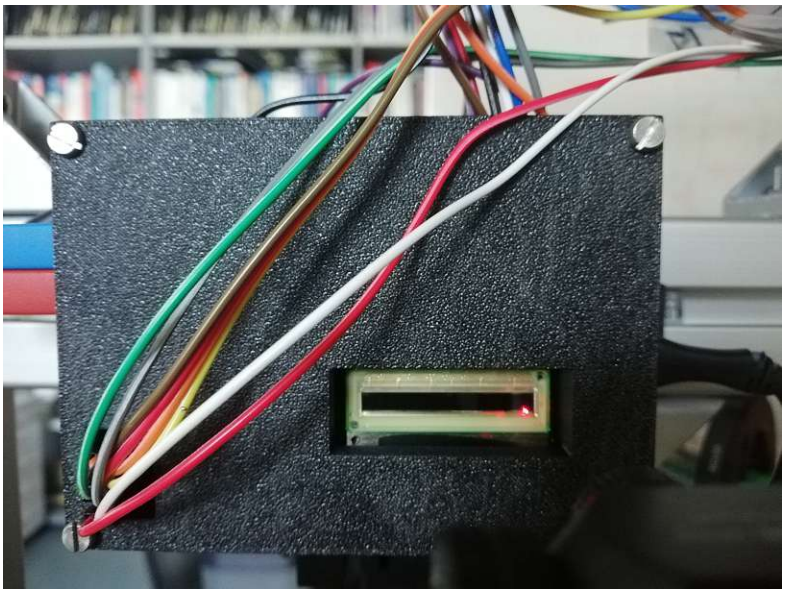

Figure 3.9: Sensor prototype mounted into 3D-printed housing. It offers a secure hold and allows easy integration into various systems. The wires on the bottom left corner represent the measured shift.

CHAPTER 4

FPGA programming

The aim of this chapter is to develop a program for reading out the line sensor with variable resolution and processing the image data to calculate the speckle shift in real-time. Therefore, the following optimization considerations are based on the line sensor specifications given in [74]. The measurement rate of the in-plane sensor prototype is optimized while taking into account a reasonable Analog Digital Converter (ADC) resolution. This is achieved through a pipeline architecture of the program. Furthermore, data processing, consisting of subpixel interpolation, correlation calculation, and maximum peak search, is implemented. The aim of subpixel interpolation is to further improve the resolution of the sensor prototype. The programm is verified via simulation testbenches, by simulating the Field Programmable Gate Array (FPGA) input signals. This allows to test the functionality of the program efficiently offline. The implementation is done using the Vivado Design Suite (Xilinx Inc., San José, California, USA), with Verilog chosen as the programming language.

4.1 Architecture

The FPGA programming can be divided into three tasks, as shown in Figure 4.1. The first one is the power-on sequence, where the supply voltages for the line sensor are applied. Here, it is crucial to apply the voltage levels in a specific order to prevent latch-up problems and faulty sensor states, according to [74]. The second task is the line sensor configuration over Serial Peripheral Interface (SPI). This includes defining a divider for the pixel clock and setting the ADC

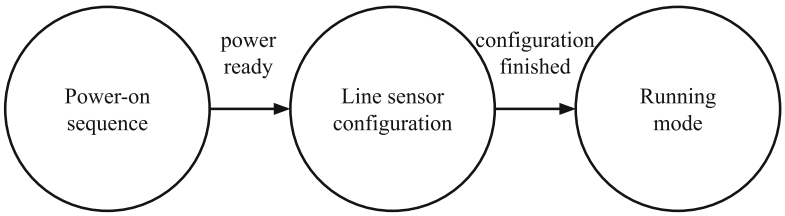

Figure 4.1: Block diagram of the FPGA program. The power-on sequence raises the power supplies for the line sensor in a specific order. The configuration of the line sensor is done via SPI. The running mode consists of the integration, conversion, readout, and pixel processing.

resolution accordingly. As higher ADC resolutions lead to longer conversion times, a tradeoff between the chosen resolution and the achieved measurement rate f has to be considered. The last task is the running mode, consisting of the integration, conversion, readout, and pixel processing. The integration time T_I is the time when photons hit the detector and charge builds up until it is transferred and stored in a hold capacitor. The time required to convert the analog pixel value into a digital one is the conversion time T_C. The readout and processing time T_R and T_P, respectively, are the times needed for reading out all the pixel values and processing a defined window of interest. An example for user-defined windows of interest is shown Figure 4.2. The red line represents the reference image, while the turquoise represents the actual subimage. To optimize the measurment rate f, the running mode is programmed fully pipelined, so that the measurment rate f is limited by the longest pipeline duration, and not by their summation. The pipelines are shown in Figure 4.3. The black pipeline consists of the integration and conversion tasks, grouped together since a new integration should never start during an active conversion, as mentioned in [74]. After the i-th integration and conversion, the i-th readout starts. Simultaneously, the (i+1)-th integration and conversion begin. The i-th image processing starts after receiving the last pixel of interest. When the (i+1)-th integration and conversion finish, the (i+1)-th readout and the (i+2)-th integration and conversion start. The procedure continues in this manner. In Figure 4.3, the measurment rate f is defined by the duration of the black pipeline, as it is the longest one. However, practically, any of these three pipelines can be the longest one, depending on the line sensor configuration, the defined window of interest, and the implemented processing algorithms. Therefore, a timing analysis is performed with the aim to optimize the measurment rate f.

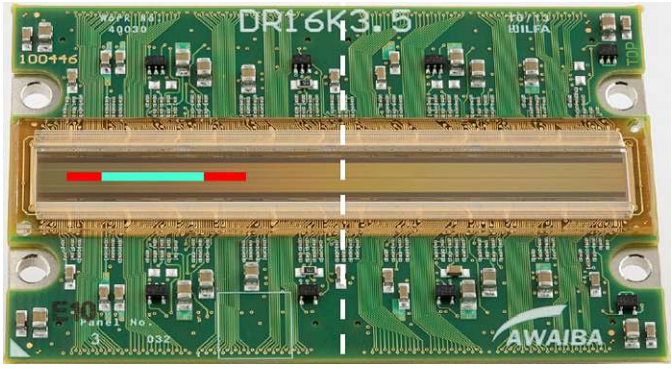

Figure 4.2: Line sensor with a user-defined region of interest [74]. The red line shows the reference image with a size of n_1 pixel, the turquoise one shows a n_2 pixel-sized subimage. The vertical dotted white line indicates that the sensor consists of two independent line segments.

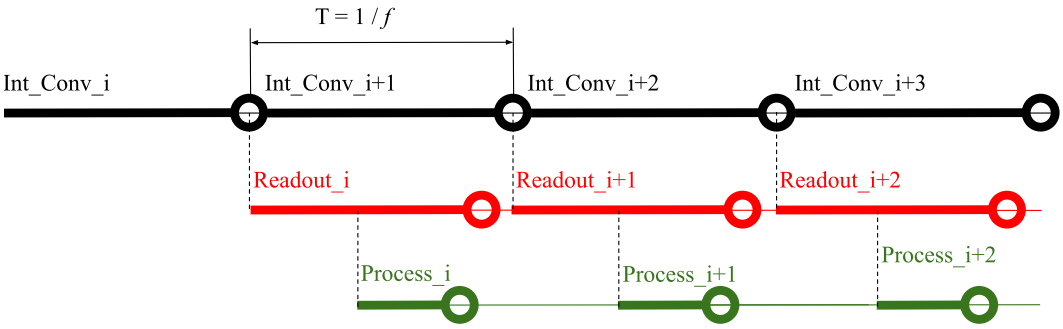

Figure 4.3: Programm architecture consisting of 3 pipelines. The black one represents the integration and conversion, the red one the readout and the green one the image processing. The achieved bandwidth depends on the duration of the longest pipeline.

4.2 Timing analysis

The resulting measurement rate of the sensor prototype is defined as

$$f \approx \frac{1}{\max(T_I + T_C, T_R, T_P)}, \tag{4.1}$$

due to the implemented pipeline architecture. In order to determine the bottleneck of the program, the minimum times regarding the sensor configuration are derived from the specifications given in [74]. The allowed minimum integration time T_I is $1\,\mu$s. The minimum conversion time T_C depends on the ADC clock and the chosen resolution. It can be written as

$$T_C = \frac{1}{f_c}(2^r - 32), \tag{4.2}$$

with r being the ADC resolution in bit and f_c being the frequency of the ADC clock. The subtraction term of 32 is required to consider that the 5 Least significant Bits (LSBs) of the ADC end-range register are set to 0 by hard wiring them to GND [74]. The maximum allowed ADC clock f_c is 100 MHz, and the resolution r can be chosen between 10 and 13 bit. For the readout, the maximum allowed pixel clock f_p is 85 MHz. Since the line sensor has only one input clock for the ADC clock f_c and the pixel clock f_p, there are 2 possibilities. Either provide the line sensor with a clock input of ≤ 85 MHz and accept a longer conversion time T_C or provide a clock input of > 85 MHz and use the on-board pixel clock divider of the line sensor, leading to a longer readout time T_R. Considering that 4160 pixel have to be read out, while 4 pixel can be read out in parallel, the readout time T_R can be written as

$$T_R = \frac{4160}{4f_p}. \tag{4.3}$$

The processing time

$$T_P = T_{Ip} + T_{Cor} + T_{Ms} \tag{4.4}$$

depends on the interpolation time T_{Ip}, the correlation time T_{Cor}, and the time T_{Ms} needed for searching the index of the maximum correlation value. A detailed discussion of the pixel processing is given in Section 4.4. Table 4.1 shows the optimal measurement rate f for various ADC resolutions r. It clearly illustrates the tradeoff between the ADC resolution r and the measurment rate f. The pixel clock f_p and ADC clock f_c are set to 85 MHz for the case of an ADC resolution r of 10 bits. Referring to Equation 4.1, this is the only case, where it makes sense to use a lower ADC clock f_c of 85 MHz. For all other cases, it has to be 100 MHz to achieve a maximum measurment rate f. The processing time T_p depends on the implemented processing algorithms. The aim is to keep the processing time T_p as

Table 4.1: Optimized measurement rate f for different ADC resolutions. The tradeoff between high ADC resolutions r and the measurement rate f is visible. An ADC resolution r of 10 bit leads to a measurement rate f of 81.7 kHz, while an ADC resolution r of 13 bit is only achievable with a measurement rate f of 12.11 kHz.

ADC resolution r in bit	10	11	12	13
ADC clock f_c in MHz	85	100	100	100
pixel clock f_p in MHz	85	50	50	50
integration time T_I in us	1	1	1	1
conversion time T_C in us	11.67	20.16	40.64	81.6
readout time T_R in us	12.24	20.8	20.8	20.8
measurement rate f in kHz	81.7	47.26	24.02	12.11

short as possible, such that it is not the performance limiting factor of the targeted in-plane sensor. With a processing time

$$T_P < \max(T_I + T_C, T_R) \tag{4.5}$$

Equation 4.1 for the measurment rate f simplifies to

$$f \approx \frac{1}{\max(T_I + T_C, T_R)}. \tag{4.6}$$

According to [76], a measurment rate of at least 2 times the highest signal frequency is needed to reconstruct the continuous signal from the discrete one. In practice, the measurment rate should be chosen approximately 5 to 10 times the highest signal frequency [77]. According to the maximum measurement rate of 81.7 kHz from Table 4.1 it follows that the sensor prototype is capable of measuring in-plane displacements of up to $81.7/2 = 40.85$ kHz or $81.7/5 = 16.34$ kHz, depending on the chosen criteria. The system's latency T_D is defined as the time it takes until in-plane displacements are visible in the system's output [78]. It can vary between

$$T_{D,min} = T_I + T_C + \tilde{T}_R + T_P \tag{4.7}$$

to

$$T_{D,max} = T_C + \tilde{T}_R + T_P + \frac{1}{f} \tag{4.8}$$

with $\tilde{T}_R$ being the shortend readout time. The shortend readout time $\tilde{T}_R$ is the time it takes to read out the line senor till the last pixel of the user-defined window. It depends on the subimage window size n_2 and on the pixel offset N_{Off} and can be written as

$$\tilde{T}_R = \frac{1}{2f_p}(N_{Off} + n_2). \tag{4.9}$$

The minimum latency $T_{D,min}$ represents the best case scenario, where target displacements a_x appear right before the integration. The maximum latency $T_{D,max}$ represents the worst case scenario, where object displacements happen right after the integration. Object displacements during the integration result in motion blur [79]. The extent of motion blur is determined by the moved object distance during the integration time T_I. Assuming an integration time T_I of 1 μs and an in-plane displacement corresponding to the pixel size of 7 μm, the object would be expected to move at a velocity of 7 m/s. According to Equation 3.5 and 3.6 the measurment range of the prototype is limited from d_{min} = -224 μm to d_{max} = 222.25 μm. Assuming that the object translates with constant acceleration from a starting point x = 0 μm with a starting velocity of v_0 = 0 m/s, an acceleration

$$a = \frac{v_{end}^2}{2x_{end}} = 110236.22\,\mathrm{m/s}^2 \tag{4.10}$$

is required to reach the end velocity v_{end} of 7 m/s at the end position x_{end} of 222.25 μm. The effect of motion blur is therefore neglected, leading to a mean latency of

$$T_D = \frac{T_{D,min} + T_{D,max}}{2}. \tag{4.11}$$

The sensor latency is characterized by the following system

$$G(s) = e^{-sT_D} \tag{4.12}$$

with s being the Laplace variable. Since the latency T_D is causing a linear phase lag it should be kept small. This is reached by minimizing the shortend readout time $\tilde{T}_R$ and the processing time T_P. The shortend readout time $\tilde{T}_R$ can be decreased by using small sized windows of interest located on the left and a small pixel offset N_{Off}, as displayed in Figure 4.2. A detailed discussion about the reduction of the processing time T_P is given in Section 4.4.

4.3 Image capture

Figure 4.4 displays the communication interface of the line sensor, consisting of multiple signals. The timing sequence and the naming of signals refer to [74]. The *pixel_clk* signal is defined by the main clock input of the line sensor and the clock divider. To initiate communication, the *reset_cvc* signal is set to zero. After a minimum delay of 1 μs, the *reset_cds* signal is driven to zero, resetting the internal reference voltages of the line sensor. Earliest after 8 clock cycles, the *sample* signal, representing the integration, is driven to logic 1 and stays high during the integration time T_I. Six clock cycles after the falling edge of the *sample* signal, the

end_adc signal drops to 0, indicating the start of ADC conversion. It stays low until the conversion time T_C expires. The *load_pulse* signal serves as the external trigger for the readout and is sent at least 4 clock cycles after the rising edge of the *end_adc* signal. When the sensor receives the trigger, readout is initiated from left to right on each segment. The rising edge of the *LVAL* signal marks the start of the readout. Pixel values are represented via the *DATA* signal, which stays high for the duration of the readout time T_R.

Figure 4.5 illustrates the implemented communication interface through a simulation testbench, incorporating the same signals as in Figure 4.4, with the addition of _AB1 and _AB2 for some of the signals, representing the two independent lines. The *DATA* signal is replaced with the 13-bit signals *TapA1*, *TapA2*, *TapB1*, and *TapB2*, as four pixels are sent in parallel with every clock cycle. At first a reference image is taken, followed by subimages, which are stored in a Lookup Table (LUT). The defined window of interest size n_1 for the reference image is chosen to be 92 pixel, and for the subimage, a width n_2 of 64 pixel is chosen. The choice is just for simulation purpose, the optimal size is discussed in Chapter 5. The pixel_offset N_{Off} is set to 100 pixel for the reference image, for the subimage its 100 + (n_1 - n_2)/2. The interpolation factor q is 1, meaning no interpolation. The calculated shift is output via the 8 bit *pixel_shift* signal. For the integration time T_I, the minimum of 1 μs is chosen. The ADC resolution r is set to 11 bit, providing double the resolution compared to the 10-bit ADC configuration. According to Table 4.1 the expected measurement rate f_{exp} equals 47.26 kHz. In Figure 4.5, the simulated measurement rate f_{sim} is 46.77 kHz. Compared to the expected one, the simulated measurement rate f_{sim} is slightly lower but still close to it. This is because Equation 4.1 neglects waiting clock cycles where nothing happens. The reduced readout time $\tilde{T}_R$ equals 1.78 μs, as expceted from Equation 4.9. The processing time T_P is 10.6 μs, as expceted from Equation 4.4, 4.13, 4.16 and 4.17. This results in a mean sensor latency T_D of 43.8 μs.

4.4 Image processing

Referring to Equation 4.7 and 4.8 the processing time T_P can influence the sensor latency T_D significantly. Therfore, the aim is to keep the processing time T_P as short as possible. This is achieved by choosing correlation and subpixel interpolation algorithms from Section 2.2.2 and 2.2.4, which allow easy FPGA implementation and offer fast performance. As written in Equation 4.4 the processing time T_P is defined by the summation of the interpolation time T_{Ip}, the correlation time T_{Cor}, and the time T_{Ms} needed for searching the index of the maximum correlation value. After the maxima search the program waits for the next subimage, before

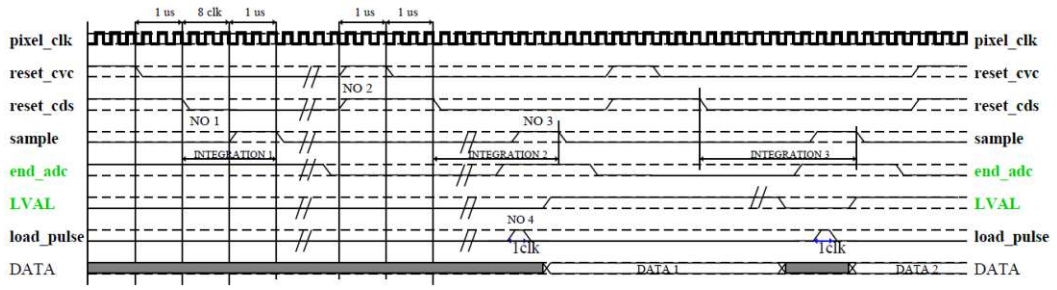

Figure 4.4: Communication interface betwenn the line sensor and FPGA for readout [74]. A high *sample* signal indicates integration, a low *end_adc* signal indicates conversion and a high *lval* signal represents valid pixel data on the output. The start of the sensor transmitting its data is performed by an external *load_pulse* trigger.

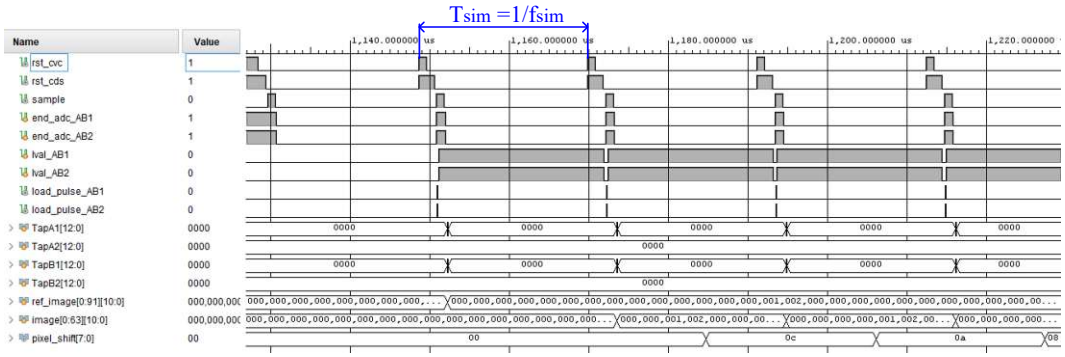

Figure 4.5: Simulated communication interface betwenn the line sensor and FPGA for readout. The sensor transmits its data over four 13 bit *Tap* signals. The pixel values are stored in a reference image at the beginning, followed by storing them in a subimage. The *pixel_shift* signal represents the calculated speckle shift.

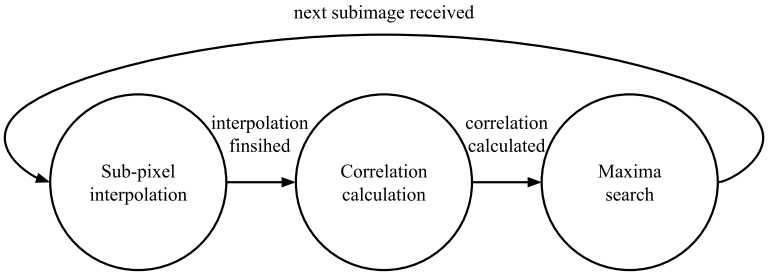

Figure 4.6: Block diagram of pixel processing. After receiving a subimage, subpixel interpolation is initiated, followed by correlation calculation and maxima search.

starting a new subpixel interpolation and correlation calculation. A block diagram is displayed in Figure 4.6. The chosen interpolation algorithm is linear pixel intensity interpolation. By making use of multiple Digital Signal Processor (DSP) slices from the Artix-7, which allows the parallel execution of calculations, it only requires 1 clock cycle to double the spatial pixel resolution. This results in the interpolation time

$$T_{Ip} = \frac{\log_2(q)}{f_{pr}} \tag{4.13}$$

with f_{pr} beeing the processing clock of 6 MHz. The chosen correlation algorithmn is cross-correlation without zero padding. This limits the size of the correlation vector to a size of $q(n_1 - n_2) + 1$. Therfore the measurment range from Equation 3.5 and 3.6 adapts to

$$d_{min} = -\frac{q(n_1 - n_2)s_p}{2q} = -\frac{(n_1 - n_2)s_p}{2} \tag{4.14}$$

and

$$d_{max} = -d_{min}. \tag{4.15}$$

The difference of the reference image size n_1 and subimage size n_2 is a tuning parameter for the measurement range. For the implementation of the cross correlation again multiple DSP slices are used, resulting in a correlation time

$$T_{Cor} = \frac{qn}{2f_{pr}}. \tag{4.16}$$

To calculate the speckle shift the index of the maximum correlation value in the correlation vector is searched. For this, the correlation vector is iterated through, and the current value is compared with the highest value encountered so far. The needed time

$$T_{Ms} = \frac{q(n_1 - n_2) + 1}{f_{pr}} \tag{4.17}$$

depends on the size of the correlation vector.

CHAPTER 5

Measurements and Results

The aim of this chapter is to evaluate the developed in-plane sensor in terms of measurement-range and rate, latency, resolution, uncertainty, crosstalk and dynamic behaviour with the use of a feedback controlled precision positioning stage. This comprehensive evaluation ensures a thorough understanding of the sensor's capabilities and limitations in real-world scenarios.

5.1 Setup

In Figure 5.1 the sensor prototype, consisting of the line sensor, FPGA, and interface board, all stacked together and enclosed within a housing, is shown. This assembly is mounted onto a support structure made from aluminum profiles and situated on an optical table. A 5V power supply is provided by the DP832 DC (RIGOL Technologies Inc., Suzhou New District, China). The object, whose in-plane displacement is measured, is the piezo stage NPXY100-100 (Motion Solutions, Irvine, California, USA), fixed to an optical table through an aluminum plate. Using the LC.402 controller (Motion Solutions, Irvine, California, USA), an open loop travel range of 160 μm as well as a closed loop range of 100 μm in both x- and y- direction can be achieved [80]. The laser placement is facilitated by an optical post assembly, comprising posts, angle clamps, a post holder, and a fork clamp. Further, the setup parameters include a detector to object distance L_o of 80 mm and a laser incidence angle θ of 20 ° relative to the object normal. The laser has a ouput power of 0.9 mW, a radius of curvature L_s of ∞, a spot diameter D of 3 mm and a laser wavelength λ of 641.5 nm. Referring to Equation 2.11, this results in

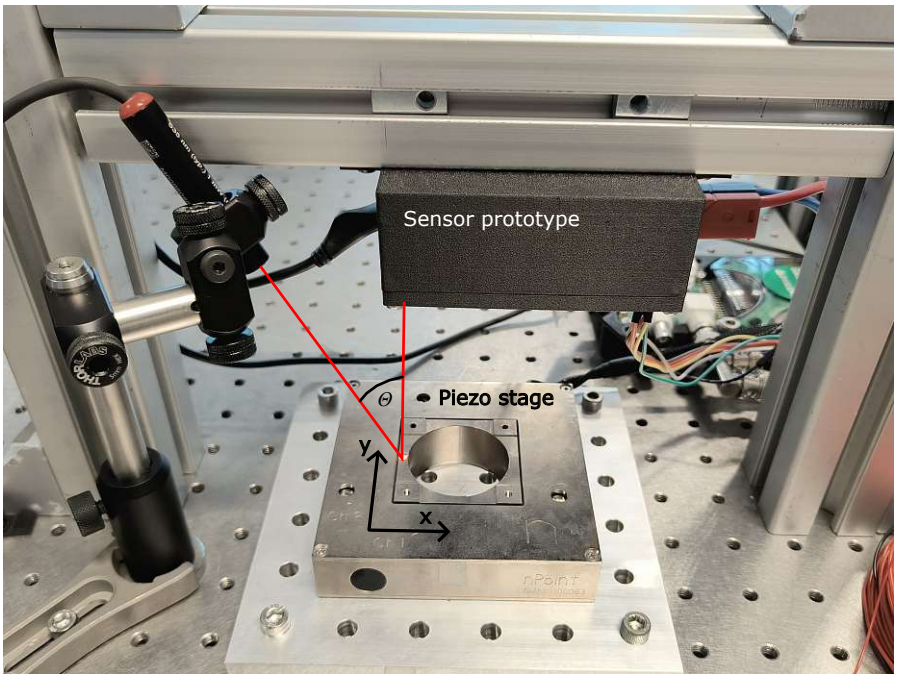

Figure 5.1: Setup to evaluate the performance of the in-plane line sensor. The sensor is mounted on a support structure made of aluminum profiles. It measures the displacement of a piezo stage in x-direction.

a mean speckle size s_{sp} of approximatly 3 pixel, large enough to prevent aliasing effects [81]. The communication interface between the line sensor and FPGA is monitored using a 4-channel oscilloscope DSO-X 4024A (RIGOL Technologies Inc., Suzhou New District, China), while the speckle shift is recorded with the MicroLabBox (dSPACE Inc., Wixom, Michigan, USA).

5.2 Evaluation

For the subsequent evaluations, the ADC resolution r of the line sensor is set to 11 bit. The integration time T_I is 20 μs, which is determined by incrementally increasing it until saturation is first observed for some pixel values. For the reference image and the current subimage, different window sizes are defined and compared. The interpolation factor q is varied from 1, meaning no interpolation, to 4, leading to a theortically achievable resolution of 1.75 μm. This results in the configurationen cases (a) - (e) as shown in Table 5.1. The pixel offset N_{Off} for the reference image is chosen to be 100 pixel, and for the subimage, it must be adjusted to 100 + (n_1 - n_2)/2. The following sections show the evaluation of the sensor prototype and describe the advantages and disadvantages for the various configuration cases.

Table 5.1: Properties of the defined configuration cases.

case	reference image size n_1	subimage size n_2	interpolation factor q
a	60 pixel	32 pixel	1
b	92 pixel	64 pixel	1
c	124 pixel	96 pixel	1
d	92 pixel	64 pixel	2
e	50 pixel	32 pixel	4

5.2.1 Computational Results

This Section presents the measurement range and latency of the sensor prototype, determined through Equations from Chapter 4. The measurement range defines the maximum detectable object displacment, while the latency is crucial for real-time applications such as in-plane position control.

5.2.1.1 Measurement range

A wide measurement range is desirable as it allows the sensor to be used for a broader range of applications. According to Equation 4.14 and 4.15 the measurement range depends on the difference of the reference image size n_1 and subimage size n_2. For this reason, the difference of the window sizes is chosen with the aim to measure the whole range of motion (160 μm for open loop) of the piezo stage in x-direction. Cases (a) - (d) have a measurement range of 196 μm, which cover the target range of motion. For case (e) the measurement range is 126 μm. Increasing the measurement range of case (e) requires a bigger reference image. Since its size is multiplied by 4, due to interpolation, the FPGA programm requires a more efficient way of saving and processing the reference image and subimage to avoid on-chip memory utilization problems and timing violations. This can be enabled by a modified sliding window architecture as presented in [82]. However, the implementation of such architecture would go beyond the scope of this thesis and is therefore not covered.

5.2.1.2 Latency

As mentioned in Section 4.2, the sensor latency T_D causes a linear phase in the sensor dynamics from the actuated stage at the input, i.e. the physical displacement of the object, to the sensor output, i.e. the measured speckle shift. If the sensor is used for in-plane position control, the linear phase lag reduces the control bandwidth. Therefore, a low sensor latency T_D is desirable. According to Equation 4.7, 4.8 and 4.11 the sensor latency T_D depends on the integration time T_I, the

Table 5.2: Calculated sensor latency for the defined sensor configurations.

configuration case	(a)	(b)	(c)	(d)	(e)
reduced readout time $\tilde{T}_R$ in μs	1.46	1.78	2.1	1.78	1.41
processing time T_P in μs	7.5	10.17	12.83	20.33	23.17
sensor latency T_D in μs	59.2	62.19	65.17	72.35	74.82

conversion time T_C, the reduced readout time $\tilde{T}_R$, the processing time T_P and the measurement rate f of the sensor. The integration time T_I, the conversion time T_C and the measurement rate f are constant for all configuration cases (a) - (e), while the remaining times vary. Table 5.2 shows the impact of the reduced readout time $\tilde{T}_R$ and the processing time T_P, on the sensor latency T_D for the defined configuration cases. The reduced readout time $\tilde{T}_R$ and the processing time T_P are derived from Equation 4.9 and 4.4, respectively. Referring to Table 5.2, the reduced readout time $\tilde{T}_R$ becomes larger for increasing window sizes, but stays below 2.1 μs for all configurations. Therfore, its impact on the sensor latency T_D can be neglected. The processing time T_P depends on the window sizes n_1 and n_2 and the interpolation factor q. Especially the subpixel interpolation increases the processing time T_P, leading to a longer latency T_D for higher values of the interpolation factor q. Configuration case (a) has the lowest sensor latency T_D of 59.2 μs, while case (e) has the highest sensor latency T_D of 74.82 μs.

5.2.2 Measurements

To determine the measurement rate, resolution, measurement uncertainty, switching uncertainty, crosstalk, and dynamic behavior of the sensor prototype, a series of measurements are conducted in the experimental setup from Figure 5.1. The results are compared against a reference measurement taken with the integrated capacitive sensor from the piezo stage.

5.2.2.1 Measurement rate

Reconstructing a continuous signal from a discrete one requires a measurement rate of at least twice the highest signal frequency [76]. In practice, measurement rates which are approximately 5 to 10 times higher than the highest signal frequency are used [77]. Therefore, a high measurement rate is desirable in order to measure high frequency in-plane displacement. According to Equation 4.1 the measurement rate of the sensor is defined by the duration of the longest FPGA pipeline. The pipelines are given by integration and conversion, readout and pixel processing. For all configuration cases (a) - (e) the summation of the integration time $T_I = 20\,\mu$s and the conversion time $T_C = 20.16\,\mu$s is the limiting pipeline, leading to

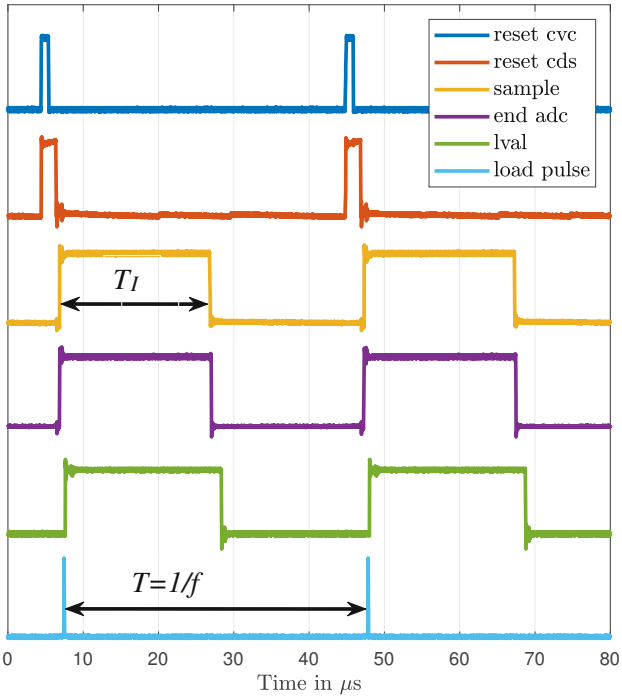

Figure 5.2: Measured communication interface betwenn the line sensor and FPGA for readout. For an integration time T_I of 20 μs, the measurement rate f of the sensor prototype is 24.72 kHz.

an expected measurement rate f_{exp} of 24.9 kHz. Figure 5.2 displays the measured communication interface between the line sensor and FPGA. The measurement rate f is 24.72 kHz, which is in good accordance with the expected measurement rate of 24.9 kHz. Considering a measurement rate 5 to 10 times higher than the maximum signal frequency [77], the sensor prototype is capable of measuring in-plane displacement of up to 4.94 kHz. With a measurement rate twice the highest signal frequency [76], in-plane displacement of up to 12.36 kHz can be measured.

5.2.2.2 Resolution

The resolution of a position sensor is defined as the minimum distance between two adjacent positions, that the sensor can reliably distinguish or detect [83]. Therefore, the theoretical resolution of the sensor prototype depends on the ratio of the pixel size of the line sensor and the interpolation factor q. This leads to a theoretical resolution for the configuration cases (a) - (c) of 7 μm, while (d) and (e) have an improved theoretical resolution of 3.5 μm and 1.75 μm, respectively.

For verification, a slow sinusoidal signal is applied to the piezo stage in x-direction with an amplitude of 49 μm (integer multiple of the pixel size) and a frequency of 1 Hz over a period of 2 cycles. The stage is feedback-controlled, operating closed-loop. Figure 5.3a visualizes the measurement result for case (a). The red signal represents the displacement measured by the prototype, while the blue signal represents the actual stage position measured by the internal capacitive sensor of the piezo stage. The difference between the signals represents the measurement error of the sensor prototype as shown in Figure 5.3a. The displacement measured by the sensor prototype aligns well with the actual stage position. However, there is a significant difference in the resolution due to the quantization steps in the displacement measured by the prototype. The resolution of the sensor prototype is experimentally evaluated by determining the height of the quantization steps, leading to a resolution of 7 μm for configuration case (a), as expected. The same procedure is applied for the remaining configurations. The measurement result for case (d) is displayed in Figure 5.3b. The quantization step height of the displacement measured by the sensor prototype reduces to 3.5 μm, which is in accordance with the expected resolution. In Figure 5.4 the measurement result for case (e) is shown. Due to the occurrence of random measurements for displacements larger than 28,μm, attributed to faster image decorrelation, the stage amplitude is reduced to 28,μm. The faster decorrelation can be explained due to systematic errors caused by the linear interpolation, as mentioned in [84]. The higher the interpolation factor q, the higher is the number of added subpixels between the real pixel values. Since the added subpixel values are all influenced by systematic interpolation errors [84], the overall error increases for higher interpolation factors q. Therefore higher order interpolation methods are suggested in digital image correlation by [85] and [84]. The effect of decreased correlation is visible in Figure 5.4 as the displacement measured by the sensor prototype is more sensitive to integer multiples of the pixel size of 7 μm. Case (e) shows variable quantization step heights ranging from 1.75 μm in the best case to 7 μm in the worst case. Consequently, the resolution decreases from the theoretical resolution of 1.75 μm to 7 μm, as it equals the minimum reliable distinction. Overall, the results indicate that the selection of an appropriate interpolation factor q plays a crucial role in the resolution and measurement accuracy of the sensor prototype. Lower values of the interpolation factor q reduce systematic errors but result in worse resolution. Higher values of the interpolation factor q can improve the resolution up to a certain point with the drawback of increasing systematic errors, and thereby introducing additional uncertainty.

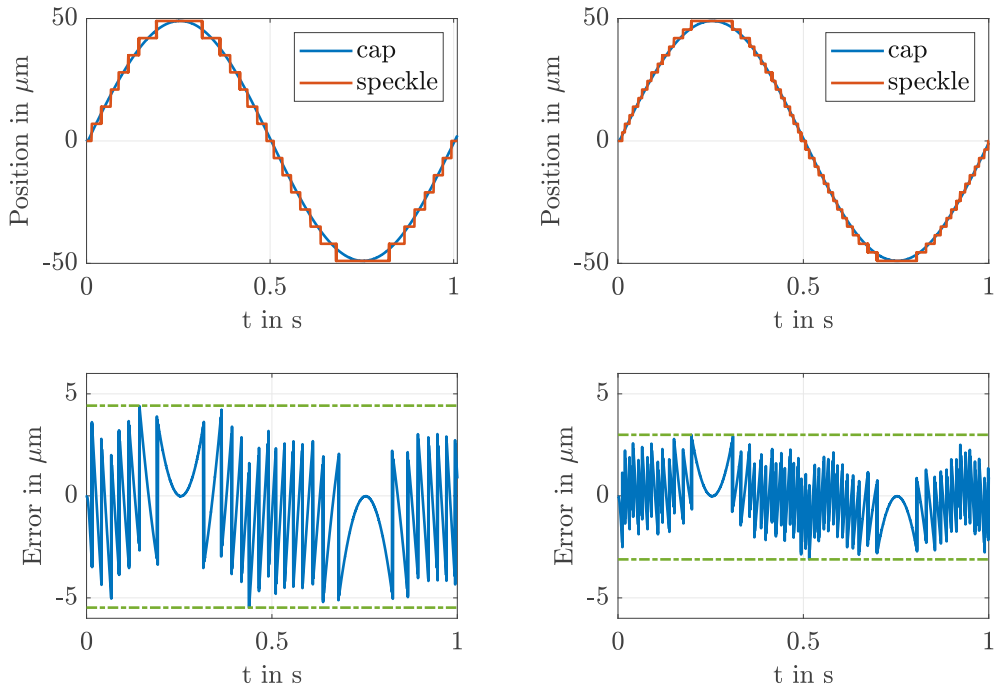

Figure 5.3: Measured displacement with configuration (a) and (d) for a sinusoidal movement with an amplitude of 49 μm and a frequency of 1 Hz. The red signal represents the displacement measured by the sensor prototype, the stage position measured by the internal capacitive sensor is shown in the blue signal. The resolution is determined by measuring the height of the quantization steps. (a) Configuration case (a) has a resolution of 7 μm and a peak to valley error of 9.9 μm. (b) Configuration case (d) has a resolution of 3.5 μm and a peak to valley error of 6.1 μm.

5.2.2.3 Measurement uncertainty

To determine the measurement uncertainty of the sensor prototype the piezo stage is actuated sinusoidal in x-direction with an amplitude of 49 μm for configuration cases (a) - (d) and an amplitude of 28 μm for case (e). The frequency is set to 1 Hz and the displacement measured by the sensor prototype and the internal capacitive sensor is recorded over a period of 10 s. The error between the two measurment principles is computed by subtracting the displacement measured by the sensor prototype from the internal stage position signal. Calculating the standard deviation of the error is then further interpreted as the measurement uncertainty σ of the prototype. Table 5.3 shows the result for the different cases.

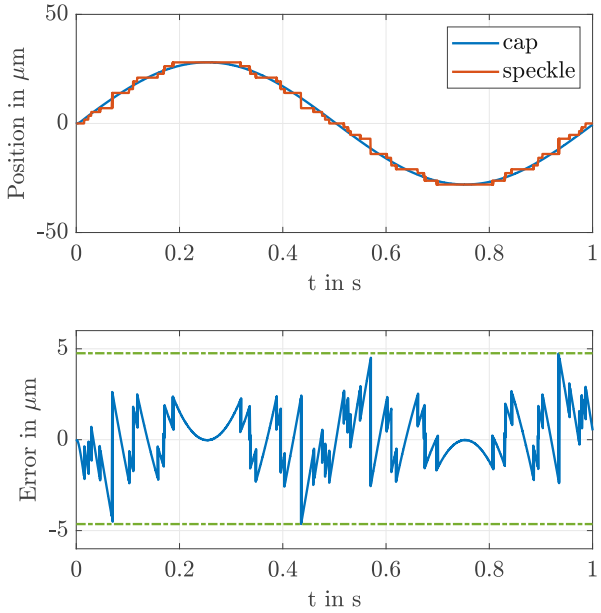

Figure 5.4: Measured displacement with configuration (e) for a sinusoidal movement with an amplitude of 28 μm and a frequency of 1 Hz. The displacement measured by the sensor prototype (red) follows the stage position from the capacitive sensor (blue) with quantization step heights ranging from 1.75 to 7 μm. The measured resolution therefore is 7 μm, the peak to valley error is 9.6 μm.

Configuration cases (a) - (c) with uninterpolated images show similar uncertainties, with slightly better performance for larger correlation windows. Their difference is attributed to increased image information for cases (b) and (c) due to bigger correlation windows, which leads to a better signal-to-noise ratio, compared to case (a). Case (d) exhibits the lowest uncertainty of approximately 1.19 μm, attributed to enhanced resolution. This is in good accordance to expectations from the error plots from Section 5.2.2.2. Case (e), with an interpolation factor q of 4 having an uncertainty of of approximately 1.41 μm. As expected, the uncertainty is greater than for case (d) but still lower compared to cases without interpolation (a) - (c).

Table 5.3: Measured uncertainty of the sensor prototype for the defined sensor configurations.

configuration case	(a)	(b)	(c)	(d)	(e)
σ_{1Hz}	2.0448	1.9970	1.9999	1.1912	1.4139

Table 5.4: Measured switching uncertainty for different configuration cases. Increasing the window size reduces the switching uncertainty, interpolation increases the switching uncertainty.

configuration case	(a)	(b)	(c)	(d)	(e)
σ_{sw} in μm	0.2885	0.1225	0.0938	0.2278	0.3966

5.2.2.4 Switching uncertainty

To determine the switching uncertainty of the sensor prototype a ramp signal with a slow slope v of 10 μm/s is applied to the piezo stage. For the configuration cases (a) - (d) the stage moves from -49 μm to 49 μm, for case (e) from -28 μm to 28 μm, all in the x-direction. The operation mode of the stage is closed loop. The displacement measured by the sensor prototype results in 14 switching points for cases (a) - (c), as visible in Figure 5.5a, 28 switching points for case (d) and 32 switching points for case (e). A switching point is characterized by a correlation maximum precisely located between two adjacent pixels. Theoretically, a switch should occur exactly when the correlation maximum can be first assigned to the neighboring pixel. However, in practice, there are multiple back and forth switches within a time period ΔT, as seen in Figure 5.5b. This results in a switching range Δs of $v\Delta T$. Subsequently, the switching range Δs is averaged over all switching points, leading to the switching uncertainty

$$\sigma_{\mathrm{sw}} = \left(\overline{\Delta s}\right) = \left(\frac{1}{N}\sum_{i=1}^{N}\Delta s_i\right) = \left(\frac{1}{N}\sum_{i=1}^{N} v\Delta T_i\right) \tag{5.1}$$

with N beeing the number of switching points. The switching uncertainty is independent from the chosen slope v as the switching time ΔT_i is proportional to $1/v$. Table 5.4 displays the switching uncertainty of the sensor prototype σ_{sw} for the different configuration cases. It can be seen that increasing the window size correlates with smaller switching uncertainties. This is because there are more distinct correlation maxima due to the improved signal-to-noise ratio. Interpolation of the images increases the switching uncertainty σ_{sw} due to systematic errors, as discussed in Section 5.2.2.2. Among the configuration cases, (c) exhibits the best performance in terms of switching uncertainty, while case (e) has the least favorable outcome.

5.2.2.5 Crosstalk

The crosstalk behaviour of the sensor prototype is analyzed with sensor configuration (d). Referring to Equation 3.3, object displacement in y- or z-direction has no effect on the speckle shift in ζ-direction. This results in crosstalk sensitivities k_{xy} and

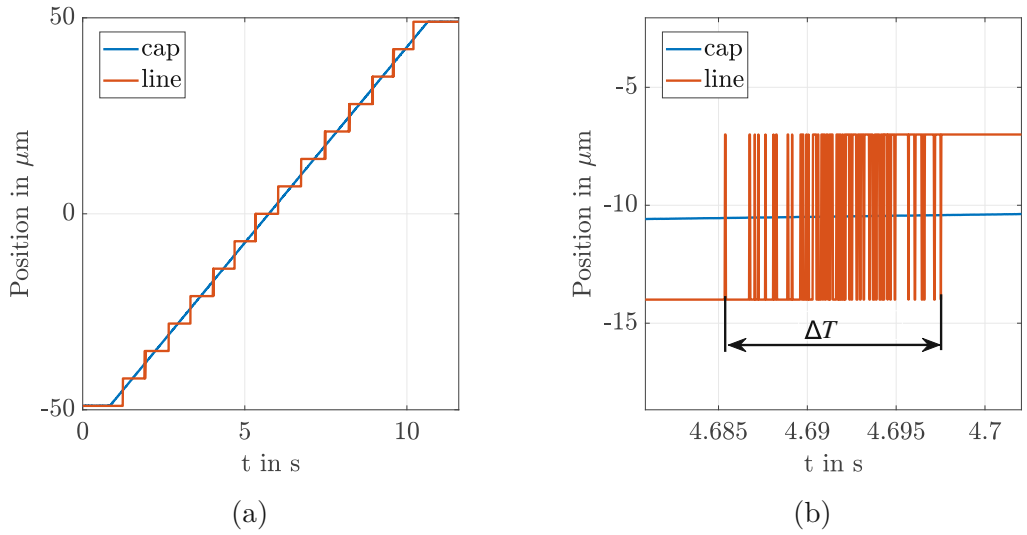

Figure 5.5: Measured switch uncertainty for configuration case (b) for a ramp signal from -49 to 49 μm with a velocity of 10 μm/s. (a) The measured displacement (red) follows the stage position (blue) with quantization steps of 7 μm. (b) Zoomed detail of switching step at stage position -10.5 μm. The measured position switches between -14 μm and -7 μm for a time of ΔT.

k_{xz} being equal to 0. However, with the line sensor's height beeing only 1 pixel an issue arises when there is a displacement in the y-direction. If the displacement in y-direction exceeds the speckle size, the reference image and subimage entirely decorrelate. To measure the crosstalk behavior of the sensor prototype, the stage is slowly moved in the positive or negative y-direction, while the x-position stays constant. The point at which the sensor prototype first outputs an incorrect x-position marks the point where correlation between the reference image and the subimage is lost, as shown in Figure 5.6a. This procedure is repeated multiple times with 27 different stage starting positions leading to 27 different reference images. Figure 5.6b displays a boxplot of the crosstalk behaviour, showing at which stage displacement y_s the above-mentioned transition occurs. The boxplot illustrates key characteristics of unknown distributions by visualizing the median, extreme values, and the variability around the median [86]. The top of the box lays at 17.18 μm and represents the 75 % boundary, while the bottom of the box, laying at 11.27 μm represents the 25 % boundary. The central mark of 13.62 μm indicates the median value. Extreme values are 6.18 μm and 21.9 μm, represented by the whiskers. By comparing the median value with the speckle size of 21 μm, it can be concluded that, correlation between the reference image and the subimage is lost at displacements in y-direction of approximately 2/3 of the speckle size.

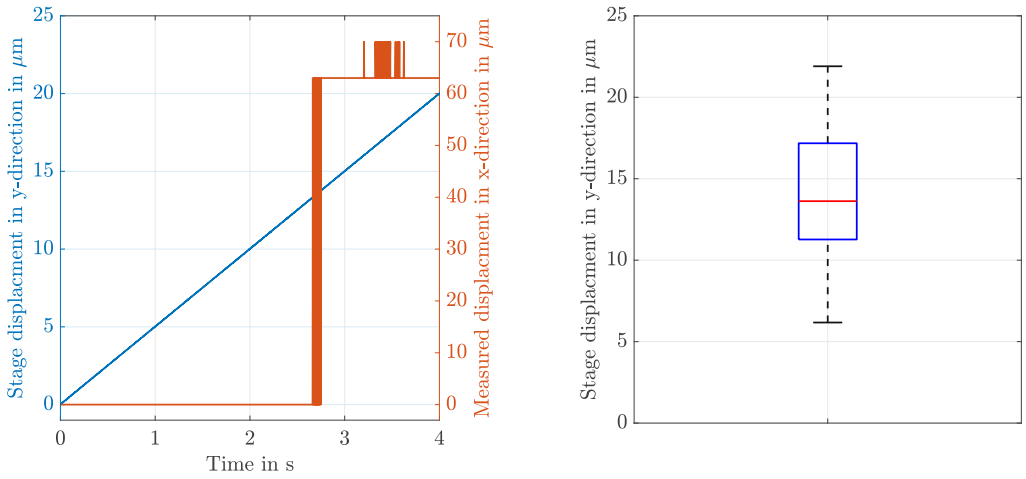

(a) (b)

Figure 5.6: Measured crosstalk behaviour of the sensor prototype. (a) The stage is moved in y-direction, while the sensor prototype measures displacement in x-direction. At a stage position y_s of 13.2 μm the sensor prototype measures a faulty x-position. This is repeated for 27 different starting positions for the stage. (b) Boxplot of the crosstalk behaviour. 50 % of the time entire decorrelation occurs between a stage postion ys of 13.62 and 17.18 μm.

5.2.2.6 Dynamic Evaluation

The dynamic evaluation involves acquiring the Bode diagram of the piezo stage with the integrated capacitive sensor and the sensor prototype. Therefore, a Network Analyzer (Analog Discovery 2, Digilent Inc., Pullman, Washington, USA) is used. This allows easy creation of the Bode plot by connecting the input voltage from the piezo stage, the displacement measured by the capacitive sensor and the displacement measured by the sensor prototype to the Analog Discovery 2. The stage input voltage and the displacement measured by the capacitive sensor are analog signals, allowing them to be directly connected. The displacement measured by the sensor prototype is digital. Therefore, it is first input in the MicrolabBox (dSPACE Inc., Wixom, Michigan, USA) via a Digital Input (DI), followed by a conversion into an analog signal with zero offset, then output via an Anaolg Output (AO) and finally connected to the Analog Discovery 2. Theoretically, this process may negatively influence the measured latency of the sensor prototype. However, with a sampling rate of 125 kHz of the MicrolabBox, the impact on the phase can be kept small. The piezo stage is operated open-loop with an input voltage of 1 V, while a frequency sweep from 0 to 1500 Hz is applied. In Figure 5.7a the measured bode plot is shown. The blue signal represents the capacitive sensor, where two resonance frequencies at 575 Hz and 955 Hz, and an anti-resonance at

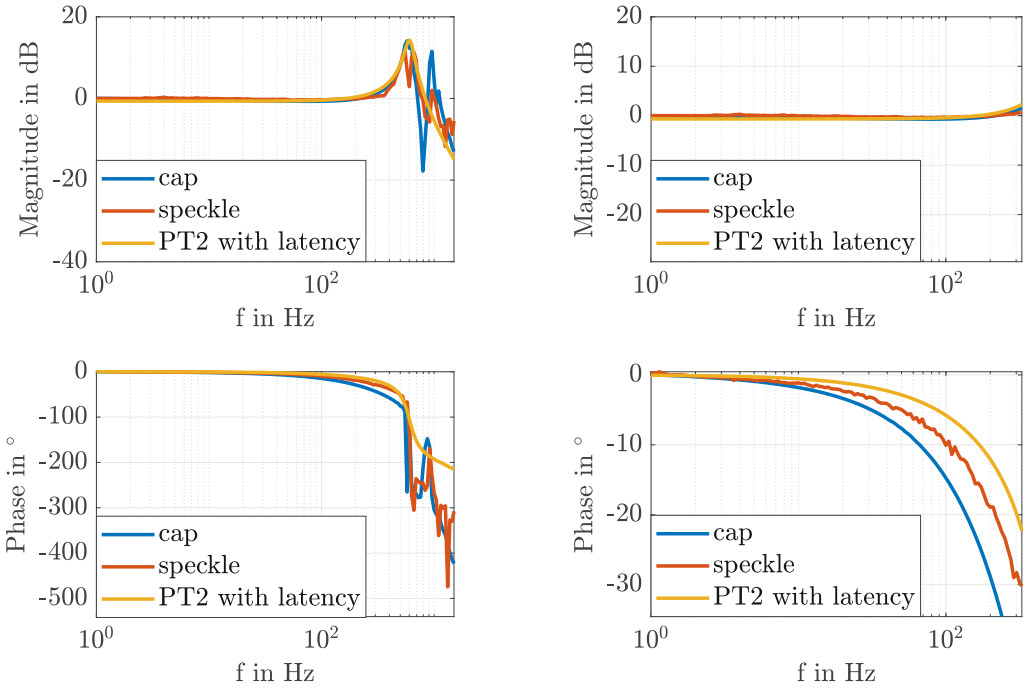

(a) (b)

Figure 5.7: Bode diagram of the piezo stage acquired with the integrated capacitive sensor and the sensor prototype. (a) Frequency sweep from 0 to 1500 Hz. The blue signal represents the capacitive sensor, the red signal represents the sensor prototype and the yellow signal approximates the piezo stage with a second order underdamped system with a latency corresponding to the calculated latency of the sensor prototype. (b) The sensor prototype has a phase lead of approximately 10 ° at 200 Hz compared to the capacitive sensor. Comparing the sensor prototpye with the approximated second order systems shows that there is addiotional latency in the system.

Table 5.5: In-plane speckle sensor specifications.

measurement range in μm	196
resolution in μm	3.5
measurement rate in kHz	24.72
measurment uncertainty in μm	1.19
latency in μs	72.35

794 Hz, are observed. The red signal represents the sensor prototype, which only shows one resonace at 575 Hz. The yellow signal approximates the piezo stage with a second order underdamped system. Additionally a latency of 72.35 μs, what corresponds to the calculated latency of the sensor prototype, is added to the yellow signal. Accoring to Figure 5.7b the sensor prototype exhibits a phase lead to the displacement measured by the capacitive sensor of approximately 10 ° at 200 Hz. Comparing the phase of the approximated signal with the phase of the sensor prototype shows a difference of 6.7 ° at 200Hz, which means that the latency of the prototype is not the only latency in the system. The measurment shows additional latency of approximately 93 μs, which can be explained through latency from conversion and from the stage controller.

5.2.3 Summary

Configuration cases (a) - (d) have a measurement range of 196 μm, while case (e) has a reduced range of 126 μm. All cases operate at a measurment rate of 24.72 kHz. Considering the sensor latency, case (a) has the best performance with a latency T_D of 59.2 μs, whereas case (e) has the longest latency T_D of 74.82 μs. Although configuration case (e) offers an improved theoretical resolution of 1.75 μm, practical measurements indicate a reliable resolution of 7 μm, consistent with cases (a) - (c). According to resolution and uncertainty case (d) stands out with the best performance, featuring a resolution of 3.5 μm and an uncertainty of approximately 1.19 μm. Switching uncertainties remain in the nanometer range across all cases and do not significantly influence the choice of optimal configuration. In practical usage of the sensor prototype, a configuration with a 1x64 pixel window and an interpolation factor of 2 seems to be optimal. Therefore, the overall sensor specification for configuration (d) is summarized in Table 5.5. The develeoped sensor prototype has a measurement range of 196 μm, a resolution of 3.5 μm, a measurement uncertainty of 1.19 μm, a measurement rate of 24.72 kHz, and a latency of 72.35 μs.

CHAPTER 6

Conclusion and Outlook

In the course of this thesis, a laser speckle-based in-plane displacement sensor has been successfully developed. This chapter summarizes the overall findings and discusses the achieved sensor performance. Additionally, an outlook for potential improvements is presented, highlighting areas for future research and development.

6.1 Conclusion

The sensor prototype comprises an image sensor, interface board, FPGA, and a laser. The geometric setup is based on an OLSP setup to ensure compactness, offering the advantage of easy sensor integration into various systems and eliminating the need for additional lenses, as discussed in Section 3.1. In order to fulfill the requirments of a resolution in the micrometer range and a measurement rate up to several 10 kHz, a high-speed CMOS line sensor with a pixel size of 7 μm is used. The feasabilty of using a line sensor for measuring in-plane displacments is verfied through simulations. A FPGA program is developed for reading out the line sensor and processing the pixel data. The program is based on a comprehensive timing analysis and the selection of a suitable program architecture, aiming for high measurement rates. The sensor's performance is fully evaluated through measurements, resulting in a measurement range of 196 μm, a resolution of 3.5 μm, a measurement uncertainty of 1.19 μm, a measurement rate of 24.72 kHz, and a sensor delay of 72.35 μs. It is noted that the sensor delay of the prototype is even smaller than that of a compared capacitive reference measurement, as shown in Section 5.2.2.6. Based on the performance evaluations of the sensor prototype, the

research question formulated in Section 2.4 can be answered:

Research Question 1

Is it possible to design and build a laser speckle-based in-plane displacement sensor, which is capable of measuring with a resolution in the single micrometer range and measurement rates up to several 10kHz?

Yes, the sensor prototype is capable of measuring in-plane displacements in one Degree of Freedom (DoF) with a resolution of 3.5 μm and a measurement rate of 24.72 kHz. This is achieved by using a high speed CMOS line sensor with a pixel size of 7 μm. The usage of a line sensor instead of a 2D sensor has the advantage of increased frame rates and less computational effort, since less pixel values have to be read out and further processed.

Research Question 2

Can the resolution of the sensor be increased with subpixel interpolation methods without decreasing the measurement rate?

Yes, the resolution of 3.5 μm is achieved through linear subpixel intensity interpolation with an interpolation factor of 2. Higher interpolation factors led to increased measurement uncertainty due systematic interpolation errors [84]. The measurement rate of the sensor prototype remains 24.72 kHz since the FPGA program for readout and pixel processing is implemented in a pipeline architecture, which enables overlapping execution of multiple tasks. Since the pixel processing happens in parallel to other tasks, the measurment rate is not affected from subpixel interpolation, as desribed in Section 4.1 and 4.2. Compared to the uninterpolated cases the latency of the sensor increases between 7.18 to 13.15 μs.

6.2 Outlook

To further enhance the performance of the speckle in-plane sensor, there are several possibilities worth considering. As mentioned in Section 3.4.3, the size of the FPGA development board is primarily responsible for the overall size of the sensor prototype. To reduce the overall size, designing a custom board with a FPGA and line sensor placed on it would make the sensor prototype more compact. Another enhancement involves improving the measurement range by implementing a reset of the reference image if correlation drops below a certain threshold [19]. Alternatively, the measurement range can also be improved with the compensation-based approach, where the object motion is tracked via feedback control, leading

to zero relative displacement between the object and the sensor prototype and thereby eliminating decorrelation effects [13]. Additionally, choosing a laser with more output power can improve the measurement rate and latency of the sensor. Currently, the sensor prototype uses a 0.9 mW laser and requires a 20 μs integration time to initially saturate certain pixel values. Compared to the minimum allowed integration time of 1 μs [74] there is scope for optimization. The drawback of this is that eye safety can be lost [87]. Furthermore, the resolution of the speckle sensor can be improved through the implementation of different subpixel algorithms. However, this comes with the tradeoff of increased latency. Lastly, another improvement involves expanding the sensor's capabilities to measure two DoF. This necessitates either the use of two perpendicular line sensors or using a 2D high-speed image sensor, which requires designing and developing a new 2D sensor protoype.

Bibliography

[1] T. Uhrmann, T. Matthias, M. Wimplinger, J. Burggraf, D. Burgstaller, H. Wiesbauer, and P. Lindner, "Recent progress in thin wafer processing," *2013 IEEE International 3D Systems Integration Conference (3DIC)*, pp. 1–8, 2013.

[2] D. Imkamp, A. Gabbia, and J. Berthold, *Challenges and Trends in Manufacturing Metrology-VDI/VDE Roadmap*. Universitätsbibliothek Ilmenau, 2014.

[3] D. Imkamp, R. Schmitt, and J. Berthold, "Blick in die Zukunft der Fertigungsmesstechnik," *tm - Technisches Messen*, vol. 79, no. 10, pp. 433–439, 2012.

[4] F. Blais, "Review of 20 years of range sensor development," *Journal of electronic imaging*, vol. 13, no. 1, pp. 231–243, 2004.

[5] Y. Dong and B. Pan, "A review of speckle pattern fabrication and assessment for digital image correlation," *Experimental Mechanics*, vol. 57, pp. 1161–1181, 2017.

[6] X. Ren, X. Xu, F. Yuan, Z. Yin, and X. He, "Semantic speckle: An auto-located speckle pattern for DIC measurement," *Appl. Opt.*, vol. 61, no. 24, pp. 7181–7188, Aug. 2022.

[7] M. Grédiac, B. Blaysat, and F. Sur, "On the optimal pattern for displacement field measurement: Random speckle and DIC, or checkerboard and LSA?" *Experimental Mechanics*, vol. 60, pp. 509–534, 2020.

[8] M. Grediac, B. Blaysat, and F. Sur, "Comparing several spectral methods used to extract displacement fields from checkerboard images," *Optics and Lasers in Engineering*, vol. 127, p. 105 984, 2020.

[9] Q. Bouyra, B. Blaysat, H. Chanal, and M. Grédiac, "Using laser marking to engrave optimal patterns for in-plane displacement and strain measurement," *Strain*, vol. 58, no. 2, e12404, 2022.

[10] X. Zhang, Y. Chi, L. Yu, Q. Wang, and B. Pan, "Laser speckle DIC revisited: An improved calculation scheme for large deformation measurement," *Optics & Laser Technology*, vol. 168, p. 109 913, 2024.

[11] R. Jones and C. Wykes, *Holographic and speckle interferometry*. Cambridge university press, 1989.

[12] M. C. Dudescu, "Optical Methods in Experimental Mechanics of Solids," *Technical University of Cluj-Napoca, Cluj-Napoca, Romania*, 2015.

[13] E. Csencsics, "Integrated compensation-based laser sensor system for in-plane and out-of-plane target tracking," *Applied Optics*, vol. 59, no. 20, pp. 6138–6147, 2020.

[14] M. Farsad, C. Evans, and F. Farahi, "Robust sub-micrometer displacement measurement using dual wavelength speckle correlation," *Optics Express*, vol. 23, no. 11, pp. 14 960–14 972, 2015.

[15] R. Paris, M. Melik-Merkumians, and G. Schitter, "Probabilistic absolute position sensor based on objective laser speckles," *IEEE Transactions on Instrumentation and Measurement*, vol. 65, no. 5, pp. 1188–1196, 2016.

[16] M. Sjödahl, "Accuracy in electronic speckle photography," *Applied Optics*, vol. 36, no. 13, pp. 2875–2885, 1997.

[17] I. Yamaguchi, "A laser-speckle strain gauge," *Journal of Physics E Scientific Instruments*, vol. 14, no. 11, pp. 1270–1273, 1981.

[18] S. Schneider, Y. Gautam, and B. Zagar, "Application of a locally operating laser-speckle strain sensor," *IEEE Transactions on Instrumentation Measurement*, vol. 52, no. 4, pp. 1025–1029, 2003.

[19] T. O. Charrett, Y. K. Bandari, F. Michel, J. Ding, S. W. Williams, and R. P. Tatam, "A non-contact laser speckle sensor for the measurement of robotic tool speed," *Robotics and Computer-Integrated Manufacturing*, vol. 53, pp. 187–196, 2018.

[20] Y. K. Bandari, T. O. Charrett, F. Michel, J. Ding, S. W. Williams, and R. P. Tatum, "Compensation strategies for robotic motion errors for additive manufacturing," *Proceedings of Proceedings of 27th Annual International Solid Freeform Fabrication Symposium*, 2016.

[21] T. O. Charrett, S. J. Gibson, and R. P. Tatam, "Application and performance of laser speckle odometry applied to a mobile industrial robot," *Optical Measurement Systems for Industrial Inspection XIII*, vol. 12618, pp. 363–369, 2023.

[22] D. Francis, T. O. Charrett, L. Waugh, and R. P. Tatam, "Objective speckle velocimetry for autonomous vehicle odometry," *Applied optics*, vol. 51, no. 16, pp. 3478–3490, 2012.

[23] L. Waugh, "Speckle velocimetry for high accuracy odometry for a Mars exploration rover," *Measurement Science and Technology*, vol. 21, no. 2, p. 025 301, 2009.

[24] L. J. da Silva, D. M. Souza, D. B. de Araújo, R. P. Reis, and A. Scotti, "Concept and validation of an active cooling technique to mitigate heat accumulation in WAAM," *The International Journal of Advanced Manufacturing Technology*, vol. 107, pp. 2513–2523, 2020.

[25] A. Yogeswaran and P. Payeur, "3d surface analysis for automated detection of deformations on automotive body panels," *New Advances in Vehicular Technology and Automotive Engineering*, pp. 978–953, 2012.

[26] T.-F. Yao, A. Duenner, and M. Cullinan, "In-line dimensional metrology in nanomanufacturing systems enabled by a passive semiconductor wafer alignment mechanism," *Journal of Micro-and Nano-Manufacturing*, vol. 5, no. 1, p. 011 001, 2017.

[27] H. Schwenke, U. Neuschaefer-Rube, T. Pfeifer, and H. Kunzmann, "Optical methods for dimensional metrology in production engineering," *CIrP Annals*, vol. 51, no. 2, pp. 685–699, 2002.

[28] D. Wertjanz, E. Csencsics, J. Schlarp, and G. Schitter, "Design and control of a maglev platform for positioning in arbitrary orientations," *2020 IEEE/ASME International Conference on Advanced Intelligent Mechatronics (AIM)*, pp. 1935–1942, 2020.

[29] D. Wertjanz, E. Csencsics, T. Kern, and G. Schitter, "Bringing the Lab to the Fab: Robot-Based Inline Measurement System for Precise 3-D Surface Inspection in Vibrational Environments," *IEEE Transactions on Industrial Electronics*, vol. 69, no. 10, pp. 10 666–10 673, 2022.

[30] D. Wertjanz, E. Csencsics, and G. Schitter, "Three-DoF Vibration Compensation Platform for Robot-Based Precision Inline Measurements on Free-Form Surfaces," *IEEE Transactions on Industrial Electronics*, vol. 69, no. 1, pp. 613–621, 2022.

[31] D. Wertjanz, T. Kern, A. Pechhacker, E. Csencsics, and G. Schitter, "Robotic precision 3D measurements in vibration-prone environments enabled by active six DoF sample-tracking," *2022 IEEE/ASME International Conference on Advanced Intelligent Mechatronics (AIM)*, pp. 1441–1446, 2022.

[32] P. Bing, X. Hui-Min, X. Bo-Qin, and D. Fu-Long, "Performance of sub-pixel registration algorithms in digital image correlation," *Measurement Science and Technology*, vol. 17, no. 6, p. 1615, 2006.

[33] J. Zhang, G. Jin, S. Ma, and L. Meng, "Application of an improved subpixel registration algorithm on digital speckle correlation measurement," *Optics & Laser Technology*, vol. 35, no. 7, pp. 533–542, 2003.

[34] G. Liu, M. Li, W. Zhang, and J. Gu, "Subpixel matching using double-precision gradient-based method for digital image correlation," *Sensors*, vol. 21, no. 9, p. 3140, 2021.

[35] J. C. Dainty, *Laser speckle and related phenomena*. Springer science & business Media, 2013, vol. 9.

[36] F. Hild, B. Raka, M. Baudequin, S. Roux, and F. Cantelaube, "Multiscale displacement field measurements of compressed mineral-wool samples by digital image correlation," *Applied optics*, vol. 41, no. 32, pp. 6815–6828, 2002.

[37] J. W. Goodman, "Statistical properties of laser speckle patterns," in *Laser Speckle and Related Phenomena*. Springer Berlin Heidelberg, 1975, pp. 9–75.

[38] J. Rigden and E. Gordon, "Granularity of scattered optical maser light," *Proceedings of the Institute of Radio Engineers*, vol. 50, no. 11, p. 2367, 1962.

[39] B. Oliver, "Sparkling spots and random diffraction," *Proceedings of the IEEE*, vol. 51, no. 1, pp. 220–221, 1963.

[40] I. Hamarová, P. Smid, P. Horváth, and M. Hrabovskỳ, "Methods for determination of mean speckle size in simulated speckle pattern," *Measurement Science Review*, vol. 14, no. 3, p. 177, 2014.

[41] X.-B. Hu, M.-X. Dong, Z.-H. Zhu, W. Gao, and C. Rosales-Guzmán, "Does the structure of light influence the speckle size?" *Scientific Reports*, vol. 10, no. 1, p. 199, 2020.

[42] J. W. Goodman, "Some fundamental properties of speckle," *JOSA*, vol. 66, no. 11, pp. 1145–1150, 1976.

[43] G. Cloud, "Optical methods in experimental mechanics," *Experimental Techniques*, vol. 31, no. 2, pp. 17–19, Mar. 2007.

[44] G. Cloud, "Optical methods in experimental mechanics: Part 27: Speckle size estimates," *Experimental Techniques*, vol. 31, no. 3, pp. 19–22, 2007.

[45] I. Yamaguchi, "Speckle displacement and decorrelation in the diffraction and image fields for small object deformation," *Optica Acta: International Journal of Optics*, vol. 28, no. 10, pp. 1359–1376, 1981.

[46] E. Csencsics, T. Wolf, and G. Schitter, "Efficient framework for the simulation of translational and rotational laser speckle displacement in optical sensor assemblies," *Optical Engineering*, vol. 61, no. 6, p. 061 410, 2022.

[47] J. Leendertz, "Interferometric displacement measurement on scattering surfaces utilizing speckle effect," *Journal of Physics E: Scientific Instruments*, vol. 3, no. 3, p. 214, 1970.

[48] P. Hariharan, B. F. Oreb, and T. Eiju, "Digital phase-shifting interferometry: A simple error-compensating phase calculation algorithm," *Applied optics*, vol. 26, no. 13, pp. 2504–2506, 1987.

[49] K. Creath, "Phase-shifting speckle interferometry," *Applied Optics*, vol. 24, no. 18, pp. 3053–3058, 1985.

[50] C.-C. Kao, G.-B. Yeh, S.-S. Lee, C.-K. Lee, C.-S. Yang, and K.-C. Wu, "Phase-shifting algorithms for electronic speckle pattern interferometry," *Applied optics*, vol. 41, no. 1, pp. 46–54, 2002.

[51] H. Fan, J. Wang, and Y. Tan, "Simultaneous measurement of whole in-plane displacement using phase-shifting ESPI," *Optics and lasers in Engineering*, vol. 28, no. 4, pp. 249–257, 1997.

[52] J. Heikkinen and G. Schajer, "Low-coherence light source design for ESPI in-plane displacement measurements," *Optics and Lasers in Engineering*, vol. 100, pp. 77–81, 2018.

[53] A. Moore and J. Tyrer, "An electronic speckle pattern interferometer for complete in-plane displacement measurement," *Measurement Science and Technology*, vol. 1, no. 10, p. 1024, 1990.

[54] F. Chen, W. Luo, M. Dale, A. Petniunas, P. Harwood, and G. Brown, "High-speed DIC and related techniques: Overview and its application in the automotive industry," *Optics and Lasers in Engineering*, vol. 40, no. 5-6, pp. 459–485, 2003.

[55] M. Shellabear and J. Tyrer, "Application of DIC to three-dimensional vibration measurements," *Optics and Lasers in Engineering*, vol. 15, no. 1, pp. 43–56, 1991.

[56] D. Kennedy, Z. Schauperl, and S. Greene, "Application of ESPI-method for strain analysis in thin wall cylinders," *Optics and lasers in engineering*, vol. 41, no. 3, pp. 585–594, 2004.

[57] L. Yang and A. Ettemeyer, "Strain measurement by three-dimensional electronic speckle pattern interferometry: Potentials, limitations, and applications," *Optical Engineering*, vol. 42, no. 5, pp. 1257–1266, 2003.

[58] D. Chen, F.-P. Chiang, Y. Tan, and H. Don, "Digital speckle-displacement measurement using a complex spectrum method," *Applied optics*, vol. 32, no. 11, pp. 1839–1849, 1993.

[59] B. Pan, K. Qian, H. Xie, and A. Asundi, "Two-dimensional digital image correlation for in-plane displacement and strain measurement: A review," *Measurement science and technology*, vol. 20, no. 6, p. 062 001, 2009.

[60] M. Hassaballah, A. A. Abdelmgeid, and H. A. Alshazly, "Image features detection, description and matching," *Image Feature Detectors and Descriptors: Foundations and Applications*, pp. 11–45, 2016.

[61] S. A. K. Tareen and Z. Saleem, "A comparative analysis of sift, surf, kaze, akaze, orb, and brisk," *2018 International conference on computing, mathematics and engineering technologies (iCoMET)*, pp. 1–10, 2018.

[62] T. O. Charrett, K. Kotowski, and R. P. Tatam, "Speckle tracking approaches in speckle sensing," *Optical Sensors 2017*, vol. 10231, pp. 97–104, 2017.

[63] T. Charrett and R. Tatam, "Performance and analysis of feature tracking approaches in laser speckle instrumentation," *Sensors*, vol. 19, no. 10, p. 2389, 2019.

[64] J. P. Lewis, "Fast normalized cross-correlation," *Vision Interface*, vol. 95, p. 120, 1995.

[65] M. Sjödahl and L. Benckert, "Electronic speckle photography: Analysis of an algorithm giving the displacement with subpixel accuracy," *Applied Optics*, vol. 32, no. 13, pp. 2278–2284, 1993.

[66] T. O. Charrett, T. Kissinger, and R. P. Tatam, "Workpiece positioning sensor (wpos): A three-degree-of-freedom relative end-effector positioning sensor for robotic manufacturing," *Procedia CIRP*, vol. 79, pp. 620–625, 2019.

[67] R. Paris, T. Thurner, and G. Schitter, "Compensation based displacement measurement using objective laser speckles," *IFAC Proceedings Volumes*, vol. 46, no. 5, pp. 264–270, 2013.

[68] I. Yamaguchi, "Automatic measurement of in-plane translation by speckle correlation using a linear image sensor," *Journal of Physics E: Scientific Instruments*, vol. 19, no. 11, p. 944, 1986.

[69] M. El-Desouki, M. J. Deen, Q. Fang, L. Liu, F. Tse, and D. Armstrong, "CMOS image sensors for high speed applications," *Sensors*, vol. 9, no. 1, pp. 430–444, 2009.

[70] S. Kleinfelder, Y. Chen, K. Kwiatkowski, and A. Shah, "High-speed CMOS image sensor circuits with in situ frame storage," *IEEE Transactions on Nuclear Science*, vol. 51, no. 4, pp. 1648–1656, 2004.

[71] D. D. Postnov, X. Cheng, S. E. Erdener, and D. A. Boas, "Choosing a laser for laser speckle contrast imaging," *Scientific reports*, vol. 9, no. 1, p. 2542, 2019.

[72] S. B. Paurazas, J. R. Geist, F. E. Pink, M. M. Hoen, and H. R. Steiman, "Comparison of diagnostic accuracy of digital imaging by using CCD and ESPI sensors with E-speed film in the detection of periapical bony lesions," *Oral Surgery, Oral Medicine, Oral Pathology, Oral Radiology, and Endodontology*, vol. 89, no. 3, pp. 356–362, 2000.

[73] Thorlabs Inc., *PL204-SpecSheet*, `https://www.thorlabs.com/drawings/6416b622fcf7a6c9-838ACF6A-A2B6-C52D-B4C2182639FBD5D9/PL204-SpecSheet.pdf`, Accessed: 21.12.2023, 2023.

[74] amsOSRAM AG, *Dragster-Product Document*, `https://ams.com/documents/20143/36005/Dragster_DS000444_2-00.pdf/d40c7f4d-873a-650f-3cc0-b9efcf132dfb`, Accessed: 21.12.2023, 2017.

[75] Numato Systems Pvt Ltd., *Neso Artix 7 FPGA Development Board*, `https://numato.com/docs/neso-artix-7-fpga-development-board/`, Accessed: 21.12.2023, 2023.

[76] C. E. Shannon, "Communication in the presence of noise," *Proceedings of the IRE*, vol. 37, no. 1, pp. 10–21, 1949.

[77] E. Schrüfer, L. M. Reindl, and B. Zagar, *Elektrische Messtechnik: Messung elektrischer und nichtelektrischer Größen*. Carl Hanser Verlag GmbH Co KG, 2022.

[78] Q.-C. Zhong, *Robust control of time-delay systems*. Springer Science & Business Media, 2006.

[79] A. Lavatelli and E. Zappa, "A displacement uncertainty model for 2-D DIC measurement under motion blur conditions," *IEEE Transactions on Instrumentation and Measurement*, vol. 66, no. 3, pp. 451–459, 2017.

[80] Motion Solutions, *NPXY100-100 High precision piezo stage*, `https://www.motionsolutions.com/stage/npxy100-100/#specifications`, Accessed: 22.12.2023.

[81] P. Reu, "All about speckles: Aliasing," *Experimental Techniques*, vol. 38, no. 5, pp. 1–3, 2014.

[82] M. Qasaimeh, J. Zambreno, and P. H. Jones, "A modified sliding window architecture for efficient bram resource utilization," *2017 IEEE International Parallel and Distributed Processing Symposium Workshops (IPDPSW)*, pp. 106–114, 2017.

[83] A. J. Fleming, "A review of nanometer resolution position sensors: Operation and performance," *Sensors and Actuators A: Physical*, vol. 190, pp. 106–126, 2013.

[84] H. W. Schreier, J. R. Braasch, and M. A. Sutton, "Systematic errors in digital image correlation caused by intensity interpolation," *Optical engineering*, vol. 39, no. 11, pp. 2915–2921, 2000.

[85] H. Bruck, S. McNeill, M. A. Sutton, and W. Peters, "Digital image correlation using Newton-Raphson method of partial differential correction," *Experimental mechanics*, vol. 29, pp. 261–267, 1989.

[86] D. F. Williamson, R. A. Parker, and J. S. Kendrick, "The box plot: A simple visual method to interpret data," *Annals of internal medicine*, vol. 110, no. 11, pp. 916–921, 1989.

[87] J. K. Franks, "What is eye safe?" *Eyesafe Lasers: Components, Systems, and Applications*, vol. 1419, pp. 2–8, 1991.

Eigenständigkeitserklärung

Hiermit erkläre ich, dass die vorliegende Arbeit gemäß dem Code of Conduct, insbesondere ohne unzulässige Hilfe Dritter und ohne Benutzung anderer als der angegebenen Hilfsmittel, angefertigt wurde. Die aus anderen Quellen direkt oder indirekt übernommenen Daten und Konzepte sind unter Angabe der Quelle gekennzeichnet.

Die Arbeit wurde bisher weder im In- noch im Ausland in gleicher oder ähnlicher Form in anderen Prüfungsverfahren vorgelegt.

Wien, im März 2024

Tobias Wolf, BSc.